Simulation Studies of Selective Laser Melting

by

Azad Gorgis

Submitted to the

The institute for Functional Matter and Quantum Technologies (FMQ)

Master of Science (M.Sc.) in *Physics*

at the

University of Stuttgart

Supervised & Examined by

Prof. Dr. Johannes Roth

Prof. Dr. Eric Lutz

Commenced on

September 1, 2021

Completed on

September 1, 2022

To my parents.

Declaration

I hereby declare that the work presented in this thesis is entirely my own and that I did not use any other sources and references than the listed ones. Neither this work nor significant parts of it were part of another examination procedure. I have not published this work in whole or in part before.

Stuttgart, September 1, 2022

_____

Signature

Acknowledgments

Prof. Dr. Johannes Roth, I'd like to express my deepest appreciation. His unique creative view into physics offered me with major insights into this extremely hard subject of study. He was aware of the difficulties I was experiencing at various phases of the procedure and helped me step by step through the entire process.

I feel a great gratefulness to my colleague, Dr. Dominic Klein, for his persistent support and encouragement. His enthusiasm for physics science research and emphasis on it impressed me considerably. Our many discussion created new ideas, which were reflected throughout the thesis. Special thanks to Dr. Sarah Müller and Simon Kümmel for their guidance and exchange of ideas.

Contents

Abbreviations

Al Aluminum

AM Additive Manufacturing

Ar Argon

CNA Common Neighbor Analysis

EAM Embedded Atom Method

EBM Electron Beam Melting

IMD Itap Molecular Dynamics

LB Lambert-Beer

LJ Lennard-Jones

LMD Laser Metal Deposition

MB Maxwell Boltzmann

MD Molecular Dynamics

NVE Constant Volume, constant Energy ensemble

NVT Constant Volume, constant Temperature ensemble

PBC Periodic Boundary Conditions

SLM Selective Laser Melting

Abstract

The technology of SLM is used to layer three-dimensional functional components. Studying and refining the factors that influence the melting of Al layer. The layer is made up of six distinct Al atom sizes in the shape of a sphere (ball) with various diameters (40 Å, 80 Å, 160 Å, 220 Å, 440 Å, 880 Å). The simulation depends mainly on MD to simulate the melting process. Although the sample sizes change, system parameters must be scaled to accommodate two distinct sample sizes. The whole melting of the Al layer has been recorded, using both sample 1 (40 Å, 80 Å, 160 Å) and sample 2 (220 Å, 440 Å, 880 Å), where with and without Ar gas, to explore the influence of Ar in the system.

It is expected that the findings of this study will serve as a platform for further research into complex systems with several layers, and that the methodological style used in this work will serve as a model for systematic studies into other structures. In the near future, this research might aid materials design for next-generation in 3D printing.

Chapter 1

Introduction

In the last decade, AM has risen to prominence as a modern manufacturing paradigm, resulting in a proliferation of materials that can be processed, reductions in manufacturing cost and time, and realization of extremely complex part geometries that were previously beyond the capabilities of subtractive manufacturing [1]. SLM, a laser based AM technology for fabricating metallic components from the fusing of metallic powder bed, has piqued the interest of the biomedical, automotive, and aerospace sectors because of its capacity to construct high-precision end-use products and shorten manufacturing process stages [2]. Aside from feed-stock material properties like particle size distribution and shape, laser processing parameters have a big impact on the end part's structure and quality. The primary SLM processing parameters that affect the energy input to the powder bed are laser power, laser spot size, scan speed, hatch spacing, hatch style, and layer thickness Figure 1.1 [3]. SLM can now create functional components from powders of just a few commercial alloy systems, such as Titanium, Nickel, Aluminum, Iron, Tungsten, and Gold [2].

Aluminum, along with Titanium, Tungsten, and Gold, is one of the most commonly used metals in micro-fabrication. Because of their high strength to weight ratio, form-ability, and corrosion resistance, Al alloys are widely employed in the automotive, aircraft, and biomedical sectors. Making geometrically complicated Al components is difficult using traditional production methods such as machining, casting, forming, and powder metallurgy. Furthermore, because of their modest cooling rates, these processes result in the creation of a coarse microstructure. Mechanical milling and subsequent consolidation of metal powders, on the other hand, may yield exceedingly thin micro-structures, even nano-crystalline material. The yield

strength of a hot isostatic pressed sample of milled Al powder of 60 nm size was 592 MPa [4]. Another research that consolidated milled nano-crystalline powder found a compressive yield strength of around 400 MPa [5]. Controlled consolidation of Al nano-powders is a tried and true technology for producing high strength nano-crystalline Al, but it lacks the ability to make useful complex pieces [6].

The melting and solidification of powder particles are affected by a combination of several characteristics. SLM, like other laser-processing methods, is characterized by high cooling rates in the order of 10^3 to 10^4 K/s, which result from the high energy input to relatively small areas on the powder bed. Despite the fact that the high thermal conductivity, reflectivity, and oxide formation propensity of Al powders make SLM more difficult than that of stainless steels or Titanium alloys, studies have demonstrated that very dense components may be created by SLM of Al powders [7, 8]. The anomalously greater yield strength and hardness attributed to SLM treated metals are attributable to the finer micro-structure and high dislocation density caused by increased cooling rates during solidification [9]. MD modeling is a powerful tool for describing the deformation processes of atomic structures. They are a valuable addition to experimental approaches, offering mechanistic insight into empirically observed processes because to their extraordinary resolution in space of single atom, time, and energy. Direct comparison with experiment, on the other hand, necessitates that the boundary conditions established on the simulated system match the experimental ones. The phrase boundary condition refers to any geometrical or thermodynamic limitation imposed on the entire system throughout the simulation. Ball milling for around 18 h has been demonstrated to create nano-crystalline powders with a size of about 60 nm that are acceptable for SLM processing [6]. SLM may be used to consolidate ball milled Al nano-powders, combining the ability of SLM to construct complicated components with the high-strength capabilities of nano-crystalline Al to generate functional Al parts with exceptional mechanical properties.

A common powder-based rapid manufacturing method is relies on the SLM. SLM allows for complete powder melting, resulting in near-full density components. SLM has an advantage over EBM and LMD in terms of equipment complexity. In contrast to EBM, there is no requirement for a high vacuum chamber to direct electron beam. In contrast to LMD, there is no need for precise alignment between the powder feeding aperture and the laser beam [10, 11]. Despite the fact that SLM is a very promising method, difficulties such as balling effect, degraded surface

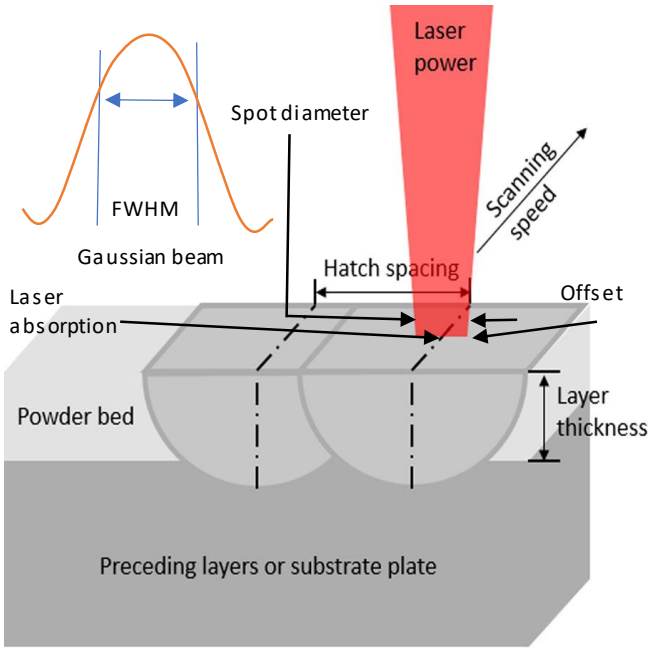

Figure 1.1: Laser power, scanning speed, hatch spacing, and layer thickness are all SLM process factors [3].

smoothness, tensile residual stress, and component deformation are still common in the SLM process because of the extreme heat input [12].

SLM processing of Al has received very little scientific attention. The SLM processing of Al powders presents a variety of challenges. For starters, SLM relies heavily on the capacity to distribute a thin powder layer, which is challenging due to the lightness and poor flow-ability of Al particles, especially in the presence of moisture. Powder bridging occurs often inside hoppers and tubes due to poor flow-ability, obstructing powder flow. As a result, many known powder deposition techniques are ineffective for Al powders, even though they are effective for other metal powders with similar particle shape and size distribution.

Despite the fact that SLM employs shorter wavelength light than selective laser sintering, which favors metal absorption, the high reflectivity of Al 91 % increases the laser power required for melting [13]. Metal powder bed lasers are generally fiber lasers with wavelengths in the 1068 to 1095 nm region and powers on the order of 100 s of Watts, for SLM machines, unpolarized IR lasers with a wavelength of 1068 nm are the industry standard [13]. Although the metal as a powder bed has a high absorptivity, many reflections and absorptions inside the particle bed represented by [14], any neighboring overlaying solidified hatch is extremely

reflective, as is the melt bead generated under the laser [15]. Another reason for greater laser powers is Al's excellent thermal conductivity relative to other materials used in SLM such as stainless Steel and Titanium [16], which allows heat to be quickly dissipated away from the scanned spot [17]. Various studies have used experimental and computational approaches to better understand the physical processes that occur during macroscale SLM processing [6]. Melting and solidification occur at very tiny length scales 10^{-3} to 10^{-8} m and time scales 10^{-6} s in the SLM process. As a result of the high cost, low resolution, and restricted accessibility of measuring tools, the experimental research of fundamental thermo-fluid-mechanical behavior is difficult.

According to the qualities, the SLM process parameters may be loosely categorized into powder related, laser related, and powder bed related factors, as depicted in Figure 1.2. In a real manufacturing setting, most powder related process characteristics, such as chemical composition, particle size and shape, and surface morphology, are invariants [18].

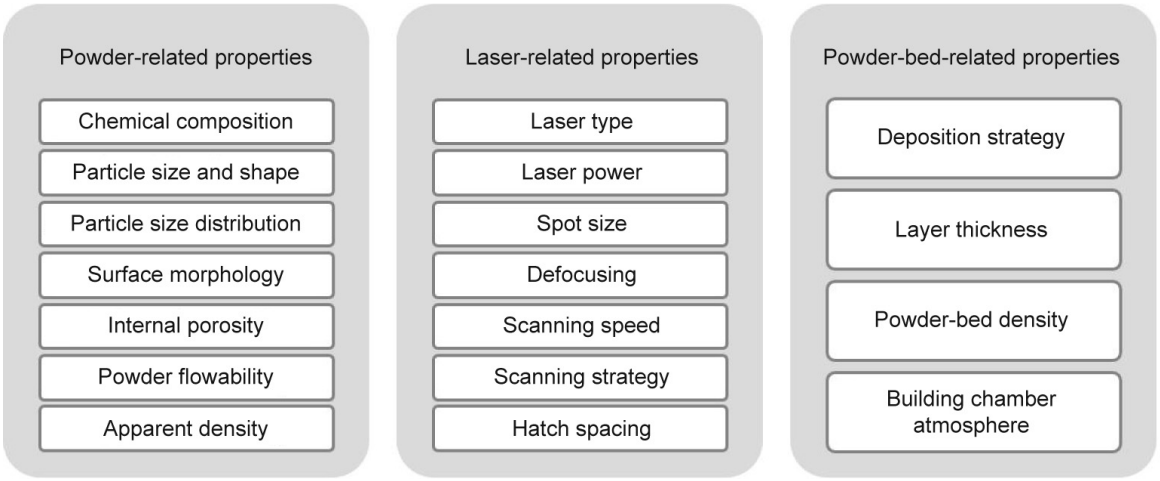

Figure 1.2: SLM process parameter summary [18].

Powder bed characteristics are the third type of SLM process parameter. Most powder bed procedures use a rake mechanism to apply the powder to the construction platform, which is also known as recoating. A variety of elements impact the effectiveness of the powder delivery system, including recoater type, number of recoating runs, amount of recovered powder during each pass, and most importantly powder characteristics. One of the important process elements that influences the component qualities is the thickness of the recoating layer. The laser material interaction, and hence the melt pool properties, are influenced by layer thickness, particle size

distribution, and laser parameters.

The SLM process setup is seen schematically in Figure 1.3. A layer of powder is initially applied to the build substrate in SLM. The laser beam melts the powder based on the geometry required. Following that, the recoater pours the next layer of powder over the hardened component, followed by further laser melting. Because of the brief contact period between the laser source and the powder, the heating and cooling rates during the SLM process are extremely high. The mechanical characteristics of the manufactured item differ from those of traditional techniques because the resulting melt pool shape has a major impact on the microstructure features. Detailed analyses of the process processes involved in SLM may be found elsewhere [19, 20]. A number of essential geometrical elements, including as the border geometry, hatch geometry, and support geometry, must be established before to the manufacture of an SLM component. These factors, together with powder absorption to laser irradiation, influence the volumetric energy density available to heat and melt the powders.

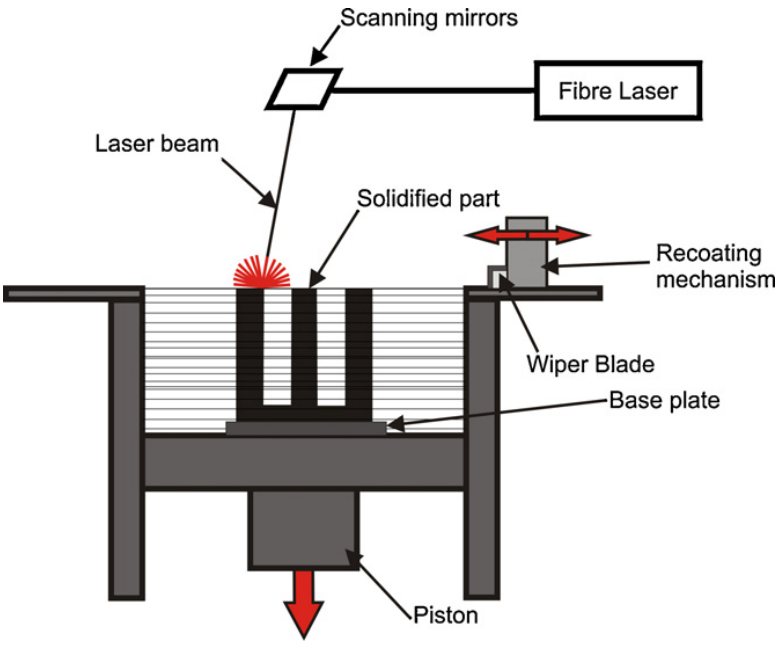

Figure 1.3: The working concept of SLM [13].

Depending on the application, the qualities of AM components created using SLM are often assessed by a range of process outputs. In order to evaluate the quality of the final produced item and therefore the SLM process, the feature resolution, surface polish, mechanical characteristics, and microstructure are characterized, as in any conventional process. There are many types of flaws that might arise in SLM. Porosity is a typical flaw in metal AM components that can

have a detrimental impact on mechanical qualities. Porosity can be powder-induced, process-induced, or a solidification artifact shown in Figure 1.4. During powder atomisation, gas pores may develop inside the powder feedstock. These spherical gas holes may be easily translated to the as-fabricated pieces [20].

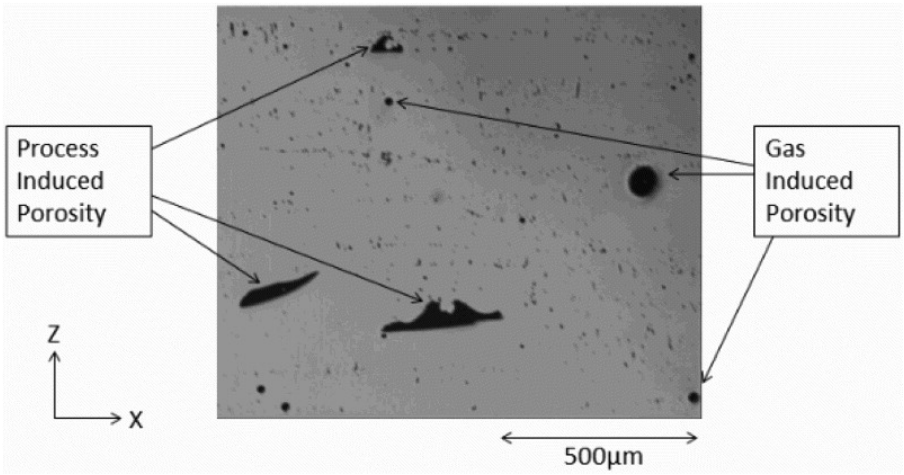

Figure 1.4: Comparison of process-induced, absence of fusion porosity to entrapped, gas porosity transmitted from the powder feedstock using light optical microscopy [20].

The production of flaws is mostly determined by the process temperature. Microstructure cracking can occur during solidification or subsequent heating. Macroscopic fractures may be associated with other flaws, such as porosity. Figure 1.5 depicts delamination leading to interlayer cracking. A combination of melt pool size and surface tension may cause swelling or melt balling if the process temperature is too high. Most of these flaws may be prevented if processing conditions are closely controlled. Cracking of the microstructure is also material dependant, and in some processing circumstances, cracking may be inevitable.

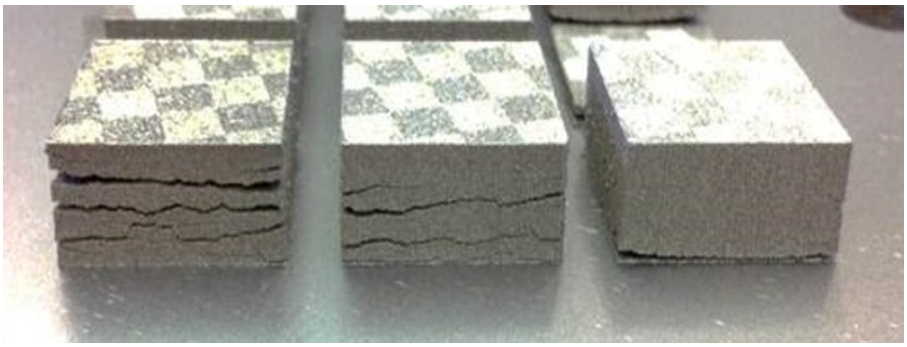

Figure 1.5: Layer delamination and cracking can occur in SLM [20].

Defect creation is mostly determined by process factors, which must be adjusted in order to create defect free components [18]. A full examination of the flaws in AM procedures may be found elsewhere [21].

Chapter 2

Theory and Methods

For simulating the development of an atomic system, classical MD simulations employ Newton's equations of motion to determine atomic locations, velocities, and accelerations. The interaction forces between two atoms are calculated using an interaction potential. An interatomic potential that accurately fits the Al melt structure, liquid properties, and crystalline properties obtained from experimental measurements and ab initio calculations is required for a reliable simulation of Al melting, grain nucleation from liquid Al, and microstructure formation. The EAM approach is a semi-empirical method for calculating metal flaws. The EAM's limitations are very well defined, it works best for purely metallic systems with no directional bonding. It does not tackle covalency or considerable charge transfer, and it does not account for Fermi-surface effects. The key physical attribute incorporated in the EAM is bond strength moderating by other bonds like coordination-dependent bond strength. Within these limits, the EAM offers a highly useful and stable method for computing estimated structure and energetics, from which many interesting metal attributes may be determined [22]. The EAM potential has previously been utilized to mimic the cooling rate dependency of liquid Al solidification [23]. The EAM approach approximates the total energy of a system of embedded atoms as,

$$E_{tot} = \sum_{i} \left[\mathbf{F}_i(\rho_i) + \frac{1}{2} \sum_{j(\neq i)} \phi(\mathbf{R}_{ij}) \right] \tag{2.1}$$

where $\mathbf{F}_i$ denotes the embedding energy of an atom i in the host electron density ρ_i and $\phi(\mathbf{R}_{ij})$ denotes the short-range electrostatic pairwise potential between atoms i and j separated by a

distance $\mathbf{R}_{ij}$. The neighbor's host electron density at atom i is estimated as follows:

$$\rho_i = \sum_{j(\neq i)} \rho_j^n(\mathbf{R}_{ij}) \tag{2.2}$$

where ρ_j^a denotes the electron density at atom i as a result of another atom separated by a distance $\mathbf{R}_{ij}$.

As a result, an accurate EAM potential developed by [24] is employed in this work to represent the interaction of pure Al atoms, and also Al with Ar. The NIST-interatomic potential repository [25] provides parameter files for the Al EAM potential that have been tuned to precisely describe the melting behavior, thermodynamic and elastic characteristics, and liquid and solid structural features.

2.1 Molecular dynamics model

MD is commonly used to simulate the time-dependent movements (trajectories) of atoms in space. Forces operating on atoms (particles) in standard MD implementations are computed as derivatives of potentials. These forces are included into Newton's equations of motion, which are solved repeatedly for each particle in the system [26]. Specifying the instantaneous positions and momenta of all the particles forming the system can describe the microstate at any time t for a classical system. There are $3\,\mathrm{N}$ coordinates $q_1, q_2, \cdots, q_{3\,\mathrm{N}}$ and $3\,\mathrm{N}$ conjugate momenta $p_1, p_2, \cdots, p_{3\,\mathrm{N}}$ for N particles. The system's Hamiltonian may be expressed in terms of these q_i's and p_i's as follows

$$\begin{aligned} H(q,p) &= K(p) + U(q) \\ q &= (q_1, q_2, \cdots, q_N) \\ p &= (p_1, p_2, \cdots, p_N) \end{aligned} \tag{2.3}$$

K and U stand for kinetic and potential energy, respectively. In the case of molecules and rigid bodies p is conjugate momenta, q is the generalized coordinate, which may be the Cartesian coordinate of each nucleus or the Cartesian coordinate of each center of mass with an orientation parameter. Kinetic energy is defined as follows:

$$K = \sum_{i=1}^{N} \sum_{\alpha} \frac{p_{i\alpha}^2}{2m_i} \tag{2.4}$$

where i is the particle number and α indicates different momenta components The potential energy U is affected by inter-molecular interactions

$$U = \sum_i \phi_1(r_i) + \frac{1}{2}\sum_i \sum_{j>i} \phi_2(r_i, r_j) + \sum_i \sum_{j>i} \sum_{k>j>i} \phi_3(r_i, r_j, r_k) + \cdots \tag{2.5}$$

where ϕ_1 is the influence of an external field on individual atoms and ϕ_2 is the pair potential, which is most relevant in computer simulation. In general, we solely examine pair potential.

We have equations of motion provided by once we know Hamiltonian information

$$m\frac{\mathrm{d}^2\vec{r}}{\mathrm{d}t^2} = -\nabla U(\vec{r}) \tag{2.6}$$

This drives the system's development and is at the heart of MD simulation. There are several numerical approaches for solving the given differential equation. The description of the inter-atomic potential $U(r)$ is a key difficulty in molecular dynamics, in the case of molecular systems, inter- and intra-molecular potential. The quality of the potential $U(r)$ has a significant impact on the accuracy and validity of the simulation results [27].

The accompanying equations of motion must be solved in order to determine the trajectories of all particles in a system with a high number of particles N,

$$m_i\vec{a}_i = \vec{F}_i \tag{2.7}$$

with

$$\vec{F}_i = \sum_{\substack{j=0 \\ j\neq i}}^{N-1} \vec{F}_{ij} = -\sum_{\substack{j=0 \\ j\neq i}}^{N-1} \nabla_i U_j = -\nabla_i U \tag{2.8}$$

where m_i is the mass of the particle i, x_i is its position vector, and $\vec{F}_i$ is its vectorial total force. Furthermore, $\vec{F}_{ij}$ represents the individual force between two particles i and j, U_i represents the potential emitted by particle the number of i, and ∇_i represents the gradient in the coordinate x_i. Because these equations of motion for particle numbers $N \geq 3$ cannot be solved analytically, numerical integration requires a simulation. This method is performed iteratively multiple times [14] to describe a certain period of time t. Figure 2.1 depicts the technique using the example of any particle in close proximity to a few additional particles. The latter exert a force on the particle under scrutiny due to their potential, and vice versa. This causes the particles' speed and direction of travel to alter, resulting in their trajectory.

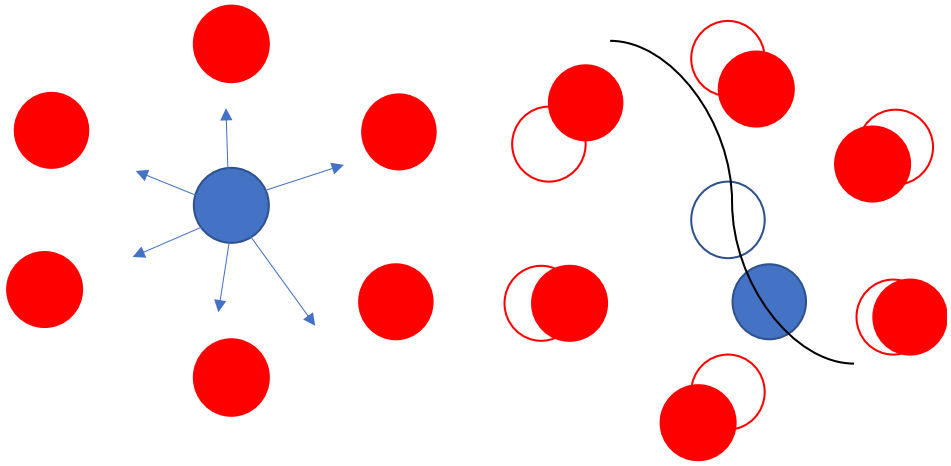

Figure 2.1: Using an arbitrary iterative integrator, a schematic depiction of trajectory creation in classical MD is shown. The total force acting on the red particle is calculated in the first step (left). The same holds true for the other particles. The following step (right) shifts all particles according to the forces acting on them, forming the trajectory of the relevant particles to a decent approximation [15].

The LJ is a well-established model potential for classical MD with uncharged particles.

$$U^{\mathrm{LJ}}(r) = 4\epsilon\left[\left(\frac{\sigma}{r}\right)^{12} - \left(\frac{\sigma}{r}\right)^{6}\right] \tag{2.9}$$

given the zero σ and the probable well depth ϵ. It has gained acceptance because the potential is analytical in nature and easily differentiable on the one hand, and it shows the interactions between two particles extremely effectively on the other. It simulates the weak but long-range Van der Waals constraint with the London force where $n = 6$ and the strong but short-range Pauli principle with a repulsion component $\sim \frac{1}{r^n}$, where $n = 12$ is frequently used for practical reasons. The potential creates a sudden repulsion of local particles on the one hand, and an attraction of more distant particles on the other, as seen in Figure 2.2.

The force exerted by particle j on particle i

$$\vec{F}_{ij} = -\nabla_i U^{\mathrm{LJ}}(\|\vec{x}_i - \vec{x}_j\|) \tag{2.10}$$

The production of the negative gradient is the outcome of the explicit usage of the potential. The LJ potential, which is solely affected by the distance r, causes a force to act along the

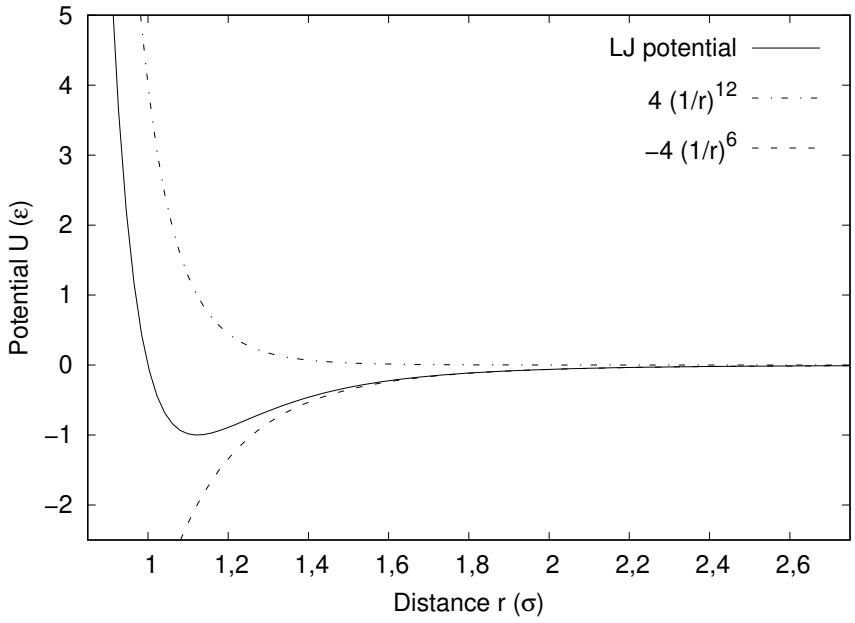

Figure 2.2: Plot of the LJ potential in parameters ϵ and σ units [28].

direction vector $\vec{r}_{ij} = \vec{x}_j - \vec{x}_i$.

$$F_{ij}(r) = 24\epsilon \frac{r_{ij}}{r^2}\left[2\left(\frac{\sigma}{r}\right)^{12} - \left(\frac{\sigma}{r}\right)^{6}\right] \tag{2.11}$$

Because each of the N particles need $N-1$ separate forces to be computed, the number of computations grows with $N(N-1)$ ($\rightarrow N^2$ for big N). Newton's Third Law states that the amount of explicit force computations may be cut in half while the scaling behavior stays quadratic.

Newton's equations of motion are numerically integrated. All iterative approaches for numerically integrating equations of motion rely on a Taylor expansion.

$$\vec{x}(t + \mathrm{d}t) = \sum_{k=0}^{\infty} \frac{\vec{x}^{(k)}(t)}{k!}\mathrm{d}t^k \tag{2.12}$$

of the trajectories centered on the point $\mathrm{d}t = 0$. In this case, $\vec{x}^{(k)}$ signifies the k-th time derivative of $\vec{x}$. One integration step t can be approximated to the next $t + \mathrm{d}t$ by discretizing the time step $\mathrm{d}t$.

The Euler technique is perhaps the simplest method of numerical integration. The trajectory's first degree Taylor polynomial is used for this

$$\vec{x}(t + \mathrm{d}t) = \vec{x}(t) + \vec{v}(t)\mathrm{d}t + O\big(\mathrm{d}t^2\big) \tag{2.13}$$

All higher orders were dropped. In this case, $\vec{v}$ represents the velocity, $\vec{a}$ the acceleration. The difficulty with Euler's technique is that it is not symplectic. As a result, the energy conservation criteria for a microcanonical ensemble cannot be satisfied [16].

The Verlet algorithm is a symplectic algorithm. It is generated by two fourth-order Taylor expansions of the trajectory, as shown in the equations Equation 2.14 and Equation 2.15, where it is valid in every situation, Taylor Expansion for the position at time t of one expansion is conducted with a positive time step $\mathrm{d}t$,

$$\vec{x}(t+\mathrm{d}t) = \vec{x}(t) + \vec{v}\mathrm{d}t + \frac{1}{2}\vec{a}\mathrm{d}t^2 + b(t)\mathrm{d}t^3 + O\big(\mathrm{d}t^4\big) \tag{2.14}$$

and the other with a negative time step $-\mathrm{d}t$,

$$\vec{x}(t-1) = \vec{x}(t) - \vec{v}\mathrm{d}t + \frac{1}{2}\vec{a}\mathrm{d}t^2 - b(t)\mathrm{d}t^3 + O\big(\mathrm{d}t^4\big) \tag{2.15}$$

Adding the two equations above and maintaining terms up to $\mathrm{d}t^2$ yields

$$\vec{x}(t+\mathrm{d}t) = 2\vec{x}(t) - \vec{x}(t-1) + \vec{a}(t)\mathrm{d}t^2 + O\big(\mathrm{d}t^4\big) \tag{2.16}$$

This is the position update equation. Similarly, we have velocity updates

$$\vec{v}(t) = \vec{x}(t+\mathrm{d}t) - \frac{\vec{x}(t-\mathrm{d}t)}{2\mathrm{d}t} \tag{2.17}$$

Equation 2.16 and Equation 2.17 are the Verlet algorithm's updating equations. Thus, the Verlet algorithm accepts as input position and acceleration at time t, as well as position at the previous time step. It is worth noting that the Verlet integrator requires the location at the "prior time step," which may be approximated as follows

$$\vec{x}(t_0 - \mathrm{d}t) = \vec{x}(t_0) - \vec{v}(t_0)\mathrm{d}t \tag{2.18}$$

The Verlet method estimates positions with an accuracy of up to $\mathrm{d}t^4$ and velocities with an accuracy of up to $\mathrm{d}t^2$. However, because it adds big and tiny values in the same equation, it is not very precise in terms of numerical precision.

$$\vec{x}(t+\mathrm{d}t) - \vec{x}(t) = \vec{x}(t) - \vec{x}(t-\mathrm{d}t) + \vec{a}(t)\mathrm{d}t^2 \tag{2.19}$$

On the left hand side, the term is of order $\mathrm{d}t$, whereas on the right hand side, the first term is of order $\mathrm{d}t^0$, the second term is of order $\mathrm{d}t^1$, and the third term is of order $\mathrm{d}t^2$.

The Velocity Verlet algorithm, which is identical to the Verlet technique, is frequently used for MD simulations, as in the simulation program IMD utilized for this work [17] used

$$\begin{aligned} \vec{x}(t+\mathrm{d}t) &= \vec{x}(t) + \vec{v}\mathrm{d}t + \frac{1}{2}\vec{a}\mathrm{d}t^2 \\ \vec{v}(t+\mathrm{d}t) &= \vec{v}(t) + \frac{\vec{a}(t) + \vec{a}(t+\mathrm{d}t)}{2}\mathrm{d}t \end{aligned} \tag{2.20}$$

By removing velocity, the basic Verlet scheme may be retrieved from these equations. This approach also necessitates the storing of 9 N bits, which represent the position, velocity, and acceleration at the current time step. Although it is not executed exactly as described above, it does include one intermediary step [27]. The first position is updated using Equation 2.16, while mid-step velocities are calculated using

$$\vec{v}(t+\frac{1}{2}\mathrm{d}t) = \vec{v}(t) + \vec{a}(t)\mathrm{d}t \tag{2.21}$$

The force and acceleration are then computed at time $t+\mathrm{d}t$, and the velocity move is computed using

$$\vec{v}(t+\mathrm{d}t) = \vec{v}(t+\frac{1}{2}\mathrm{d}t) + \frac{1}{2}\vec{a}(t+\mathrm{d}t)\mathrm{d}t \tag{2.22}$$

This is the most popular integrator choice due to its stability, precision, and simplicity. The symplectic aspect of the two methods is retained due to their equivalence, but the algorithm is now velocity-dependent. However, in traditional MD, this is not an issue because the velocities are of importance for some parameters such as the system temperature. Furthermore, it is self-starting, which implies that individual initial values are sufficient and that no initial value pairs must be formed by integration with another integrator.

2.1.1 The laser concept

When a substance is exposed to laser light, the photons excite the electrons in the material. At the minuscule penetration depth $\mathrm{d}x$, only a definite number of electrons can absorb exactly the energy of the incoming photons. Because the quantity of photons is related to the strength of the laser, the likelihood of absorption reduces as the intensity lowers. LB law's explains this tendency described

$$\begin{aligned} -\frac{\mathrm{d}I}{\mathrm{d}x} &= \mu I(x) \\ I(x) &= I(0) \cdot \exp(-\mu x) \end{aligned} \tag{2.23}$$

As a result, the quantity of excited electrons falls exponentially with laser penetration depth. The excitation of electrons causes the system to enter a state that varies from the state of equilibrium. The electron system, which was spatially non-uniformly energized, is now attempting to restore to equilibrium using thermodynamic laws. Thermalization refers to the spread of electron temperature caused by electron-electron collision interactions. Electron-phonon coupling transfers the energy of the electron system to the lattice, however it takes significantly longer than thermalization. However, because MD models individual atoms rather than electrons, the so-called rescaling model is necessary. Because thermalization occurs on a much smaller time scale than the simulation step size, the heating of the material may be described as a localized instantaneous increase in the kinetic energy of the particles.

The equipartition theorem states that the mean kinetic energy

$$\langle E_{\text{kin}} \rangle = \frac{f}{2} k_{\text{B}} T \tag{2.24}$$

$\langle E_{\text{kin}} \rangle$ is proportional to the temperature T, where f represents the number of degrees of freedom and k_{B} represents the Boltzmann constant.

The most direct application of laser heating is probably to scale particle velocities according to the velocity factor required by the equation Equation 2.24. Be the desired energy change $\mathrm{d}E$ now. It follows for the factor with $E_{\text{kin}} \sim \vec{v}^2$ with $\vec{v}(t + \mathrm{d}t) = c\vec{v}(t)$

$$\begin{aligned} c^2 &= \frac{E_{\text{kin}}(t + \mathrm{d}t)}{E_{\text{kin}}(t)} \\ c &= \sqrt{1 + \frac{\mathrm{d}E}{E_{\text{kin}}(t)}} \end{aligned} \tag{2.25}$$

Because $E_{\text{kin}}(t)$ may be readily calculated by adding up the squares of the velocities, the required energy input dE is unknown. A Gaussian intensity profile of the form is used to determine this

$$I(r) = I_0 \exp\left(-\frac{r^2}{2\sigma}\right) \tag{2.26}$$

Using the Gaussian function's variance σ a normalized Gaussian function is depicted in Figure 2.3. The width and height fluctuate inversely with the variance of σ due to normalization.

The intensity profile is only dependent on the distance r to the beam axis, according to the equation Equation 2.26 $r^2 = x^2 + y^2$ for a laser in the z direction. An integration along the plane perpendicular to the beam direction must yield the total power P_{Total} of the laser,

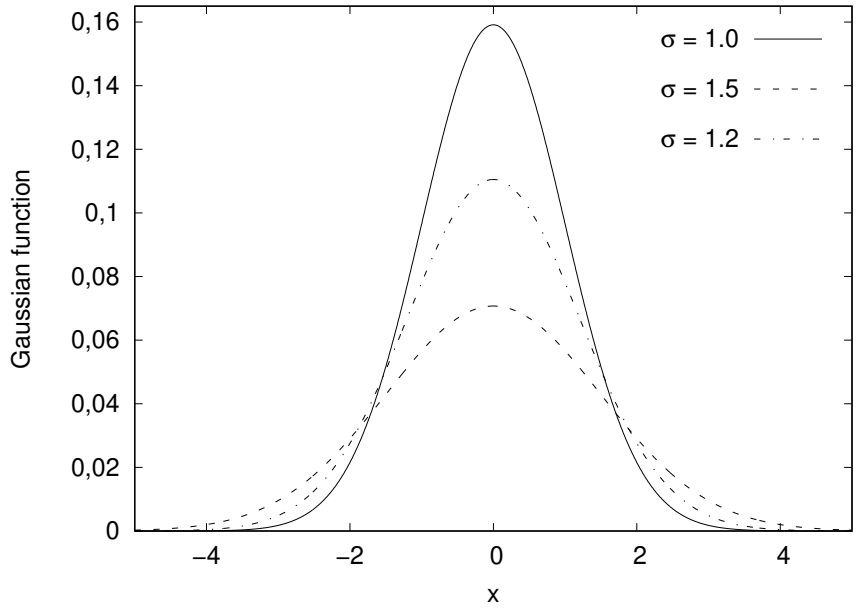

Figure 2.3: A normalized Gaussian grows larger as its width decreases and vice versa if its width changes σ.

allowing the correlation to be give

$$P_{\text{Total}} = \int_{\mathbb{R}^2} I(r)\mathrm{d}x\mathrm{d}y = I_0 \int_0^{2\pi} \mathrm{d}\theta \int_0^{\infty} \exp\left(-cr^2\right)\mathrm{d}r \tag{2.27}$$

If the variance is now written as a $FWHM = 2\sqrt{2\ln 2}\sigma$, the maximum intensity is obtained

$$I_0 = \frac{P_{\text{Total}}}{\pi} \frac{4\ln 2}{FWHM^2} \tag{2.28}$$

Because no intensity decrease has occurred in the derivation according to the LB law with the absorption μ, the intensity is multiplied by the relevant factor. The reflection coefficient R is also integrated directly

$$I(x, y, z) = \exp(-\mu z) \cdot (1 - R) \cdot I(x, y) \tag{2.29}$$

However, because the change in kinetic energy and hence the speed is required by the equation Equation 2.25 rather than the intensity, the discrete change in energy $\mathrm{d}E$ must be determined. This necessitates taking into account the amounts per discrete volume unit $\mathrm{d}V$ and each time step $\mathrm{d}t$.

$$\mathrm{d}E = \mathrm{d}I \cdot \mathrm{d}A \cdot \mathrm{d}t \tag{2.30}$$

Expanding with $\mathrm{d}z/\mathrm{d}z$ yields the form

$$\mathrm{d}E = \frac{\mathrm{d}I}{\mathrm{d}z} \cdot \mathrm{d}z \cdot \mathrm{d}A \cdot \mathrm{d}t = \frac{\mathrm{d}I}{\mathrm{d}z} \cdot \mathrm{d}V \cdot \mathrm{d}t \tag{2.31}$$

Although $\mathrm{d}I/\mathrm{d}z$ is a difference quotient, it has the same significance in the discrete setting as the derivative $\partial_z I$. This is known from the equation Equation 2.29, thus the entire expression for energy change is now

$$\mathrm{d}E = (1-R) \cdot \mu \cdot \exp(-\mu z) \cdot \frac{P_{\mathrm{Total}}}{\pi \sigma_{\mathrm{sc}}^2} \cdot \exp\left(-\frac{x^2+y^2}{\sigma_{\mathrm{sc}}^2}\right) \cdot \mathrm{d}V \cdot \mathrm{d}t \tag{2.32}$$

It should be noted that $\sigma_{\mathrm{sc}}^2 = 2\sigma^2 = FWHM^2/(4\ln 2)$ is not the variance, but merely serves as a better representation.

A simplified application of LB law's is an approximation that makes sense for reasons of easier implementation and higher processing power. While this formula takes into account the duration of the electromagnetic waves in the medium, a constant z value is assumed here for the commencement of absorption. The reason for this is that precise absorption would only be feasible by discretizing the laser into smaller sub-beams and ray tracing from there tracing. This, however, is quite computationally demanding and would have to be performed after each simulation step.

Because this approximation is accurate for geometries with a homogeneous atomic distribution in the z direction and a straight top edge (e.g., cuboid or cylindrical objects), it may be considered a good approximation for spherical arrangements. Although this causes changes in individual trajectories, a change in macroscopic attributes is unlikely to be expected because the system's dynamics stay about the same.

For the simulations that follow, the orders of magnitude are scaled down. The powder particle size in the SLM process is typically in the region of a few micrometers [29], which is challenging to achieve with the computer power available thus far [30]. As a result, a powder particle size of hundreds of Å is expected. The addition of these scaling factors results in a change in units. As a consequence of their simulation, this study group was able to demonstrate the Kelvin-Helmholtz instability at a very small number of particles. Because the emergence of this instability is significantly dependent on its starting values, it may be seen as a motivation to compress the facts to be simulated here to smaller scales, as the behavior of fluids is essentially also of interest here [31]. As with this publication, gravity must be adjusted to compensate.

2.1.2 Temperature and Pressure

It is necessary to understand how temperature and pressure are defined in MD simulation. The zeroth law of thermodynamics is used to define temperature empirically. When a material, such as mercury, comes into contact with a body at a different temperature, its thermodynamic properties, such as volume, fluctuate until it reaches a condition of thermal equilibrium, i.e. a uniform temperature. The comparison of this volume with the volume that occurs in equilibrium with a body at another, arbitrarily specified temperature yields a temperature scale that allows the temperature of a third body to be determined. Because various scales emerge based on the material attribute under consideration, whether volume, pressure, or the change in angle of the pointer of a bimetallic thermometer, and depending on the fixed points given, such a thermometer can only determine an empirical, relative temperature. Temperature ranges are mutually exclusive.

However, an instantaneous kinetic temperature may be determined using the extended uniform distribution theorem [32], applies to ergodic systems in thermal equilibrium.

$$\left\langle p_k \frac{\delta H}{\delta p_k} \right\rangle = k_B T \tag{2.33}$$

where p_k is the $k-th$ momentum component of a particle This results in for N particles with no internal degrees of freedom [33],

$$\left\langle \sum_{i=1}^{N} |\mathbf{P}_i|^2 / M_i \right\rangle = 2\langle E_{kin} \rangle = 3Nk_B T \tag{2.34}$$

Alternatively, in the case of a single atom type,

$$T = \frac{M}{3k_B} v_{rms}^2 \tag{2.35}$$

The root mean square in this case is $v_{rms}^2 = \sum_{i=1}^{N} v_i^2 / N$. Because classical particles in thermal equilibrium have a MB velocity distribution, Equation 2.35 may alternatively be written as

$$T = \frac{M}{2k_B} v_{th}^2 \tag{2.36}$$

Given the most likely MB distribution speed $v_{th} = \sqrt{2/3} v_{rms}$. As a result, up to a constant, the instantaneous kinetic temperature corresponds to the kinetic energy of a particle travelling with the most likely speed (thermal speed) v_{th} varied. Figure 2.4 depicts the MB distribution as well as the two speeds. The thermodynamic temperature is thus the time average of the

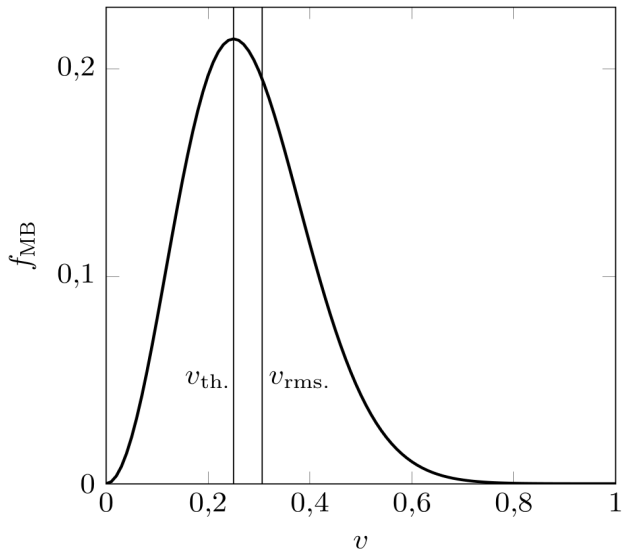

Figure 2.4: The Maxwell-Boltzmann velocity distribution is depicted schematically. The most likely (thermal) speed v_{th} is also shown. As well as the root of the mean square velocity v_{rms} [34].

instantaneous temperature for limit $t \to \infty$ Furthermore, the Virial theorem allows for the computation of an instantaneous pressure:

$$PV = Nk_BT + \langle W \rangle \tag{2.37}$$

where $\mathbf{F}_{ij}$ is the distance vector and $\mathbf{r}_{ij}$ is the Clausius Virial for N particles with pairwise additive forces

$$\langle W \rangle = \frac{1}{3} \sum_{i=1}^{N} \sum_{j>i}^{N} \mathbf{F}_{ij} \mathbf{r}_{ij} \tag{2.38}$$

This equation is true regardless of the ensemble employed as long as we are not dealing with long-range forces. The $\alpha\beta$ component of the Virial stress tensor

$$\sigma^{\alpha\beta} = \sum_{i=1}^{N} \left(\frac{V_a}{V} \right) \sigma_i^{\alpha\beta} \tag{2.39}$$

is then calculated using the i-th atom's (atomic) stress tensor

$$\sigma_i^{\alpha\beta} = \frac{1}{V_a} \left\langle -M v_i^{\alpha} v_i^{\beta} - \sum_{j>i}^{N} f_{ij} \frac{r_{ij}^{\alpha} r_{ij}^{\beta}}{r_{ij}} \right\rangle \tag{2.40}$$

The variable V_a is the mean atomic volume, v_i^{α} is the velocity vector $\mathbf{v}_i$ α component, and r_{ij} is the vector $\mathbf{r}_i - \mathbf{r}_j$ α component. These pressure and stress formulas are only applicable if the

potential, such as the EAM potential, is radially symmetrical. For three-body potentials, such as the Stillinger-Weber potential [35], alternative formulations exist. It should also be noted that the phrase atomic volume only makes sense when discussing an almost homogeneous substance. For deformed solids or surfaces, this amount is not well defined. In this situation, using a Voronoi decomposition, each atom is commonly allocated a non-overlapping Voronoi cell as the atomic volume [36].

2.2 Simulation process

2.2.1 Building the samples

All computations in this work were done with IMD [37]. For the depiction of initial atomic configurations and post-processing of MD simulations, the open visualization tool Ovito is employed [38]. IMD is used to create the sample with $make\_config$, which creates the sample configuration by building the sample bulk by specifying the size in x, y, z, the lattice constant a, the atom mass m, and the structure FCC for Al. Figure 2.5 the first atomic structures of the Al nano-powder bed, Al atoms are placed in an FCC lattice with a lattice constant of 4.0495 Å to form nano-powder particles in a simulation box with dimensions of x, y, and z, and created by different dimensions, first with $3239.6 \times 809.9 \times 1295.84$ Å and the number of atoms are $(204,800,000)$, the second one with $850.395 \times 202.475 \times 323.96$ Å with number of atoms $(3,360,000)$, and the third one with $4859.4 \times 1214.85 \times 1943.76$ Å and the number of atoms are $(691,200,000)$ along the x, y and z axes, respectively.

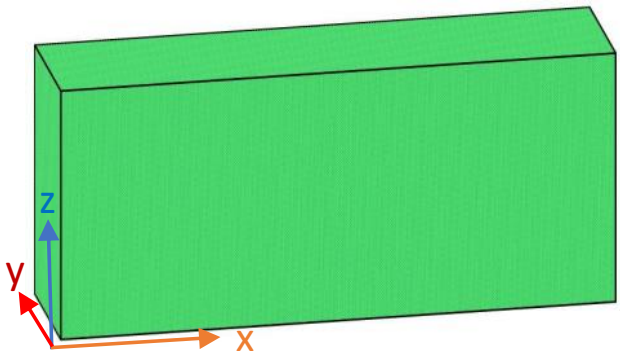

Figure 2.5: Initial configuration of the Al nano-powder bed.

Using *imd_cookie_cutter* [39] is utility for deleting atoms from IMD configuration files, to generate the sample with the ability to define the form, kinds of atoms, and atoms or layers that contributed or did not contribute to the simulation box. Figure 2.6 (a) is a first dimension structure sample with a number of atoms decreased to $(2,600,647$ after construction), and Figure 2.6 (b) the samples are the same design but with a different size box and number of atoms. The first has $850.395 \times 202.475 \times 323.96$ Å and $(357,614)$ atoms and the second has $4859.4 \times 1214.85 \times 1943.76$ Å and $(56,951,349)$ atoms, and periodic boundary conditions along the x, y and z axes, respectively.

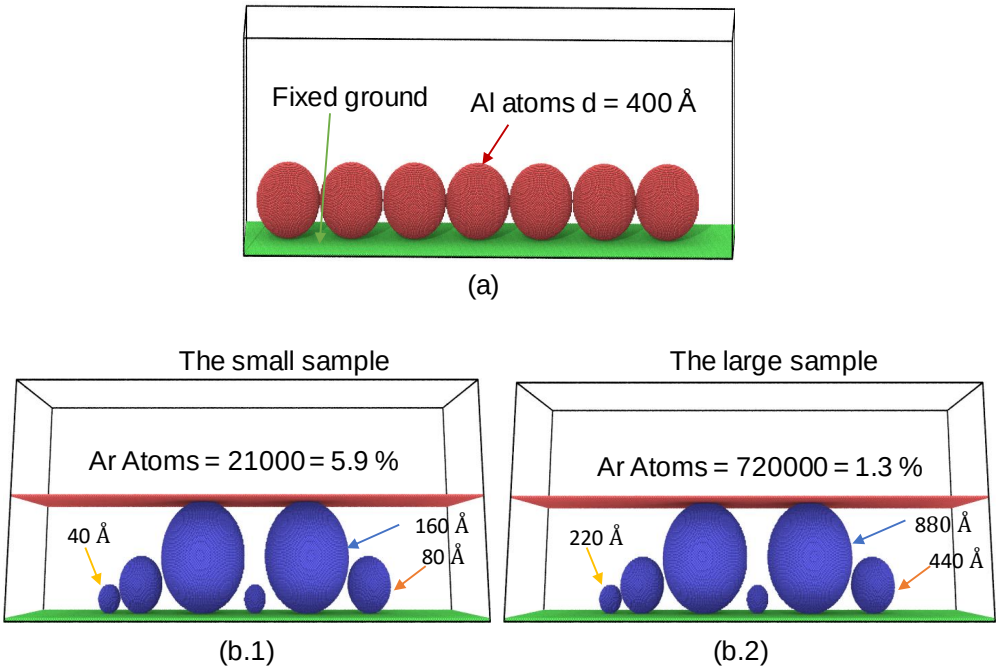

Figure 2.6: The various samples, (a) the same size balls with no Ar added to the box, (b) small and big samples with variable ball sizes and a layer of Ar in the box. where the density of Ar atoms changes in comparison to the simulated box, for the small 5.9 % and for the big 1.3 %.

Figure 2.7 depicts the basic structure position of a spherical lattice segment, and the contact area between the stationary ground and the moving balls grows.

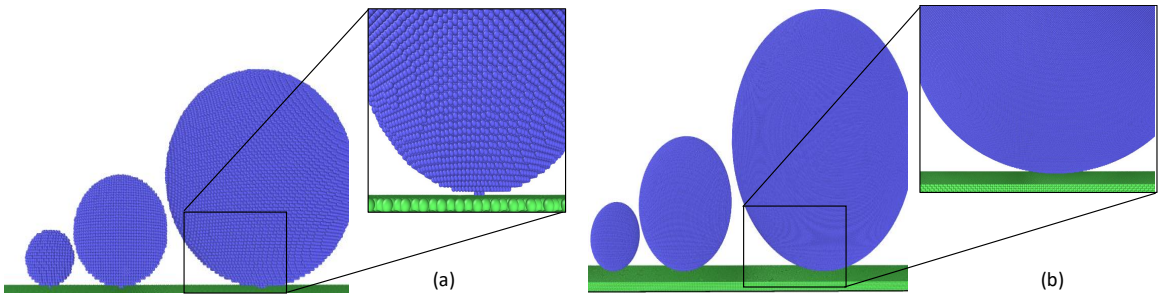

Figure 2.7: (a) small, (b) large sample density of a sphere of Al atoms (blue) on a solid and immovable surface ground (green). The contact area under the balls shows that the contacted atoms for the small one are roughly 4 atoms, whereas the contacted atoms for the large one are nearly 100 atoms.

2.2.2 Equilibration

The different samples should be equilibrated to room temperature, in IMD integrators which is the procedure that moves the atoms based on current forces and velocities. The ensemble parameter in the parameter file section 4 is used to pick the active integrator, the thermodynamic ensembles is NVT. The Berendsen thermostat is a basic one-thermostat in which the link between temperature and particle velocity defined by the equipartition theorem Equation 2.24 is utilized to globally rescale all particle velocities. This has resulted in a loss of the MB distribution of velocity magnitudes. The thermostat employed in IMD is hence the Nosé-Hoover thermostat [9, 40]. NVT with temperature coupling using a Nosé-Hoover thermostat more precisely, this is an ensemble with external temperature control and the temperature can actually vary during the simulation [9]. From starting temperature (*starttemp*) to ending temperature (*endtemp*), the enforced temperature changes linearly (defined it in parameter file section 4). (*tau_eta*) coupling time constant, determines the period of changes in temperature at equilibrium, which differs significantly from a relaxation time, is another essential value. In the parameter file, by setting the *starttemp* and *endtemp* to 0.025 eV which is equal to almost 290 K with ensemble NVT. In the case if the *tau_eta* not set and left as default the simulation will take to longer time 250 ps to be stabilized to room temperature as see it in Figure 2.8 (a), but by setting the value of *tau_eta* to 1 the simulation in earlier stage will be stabilized to 290 K in 0.5 ps as shown in Figure 2.8 (b) for the same system.

Now that the simulation box is at room temperature around 293 K, adding NVE ensemble

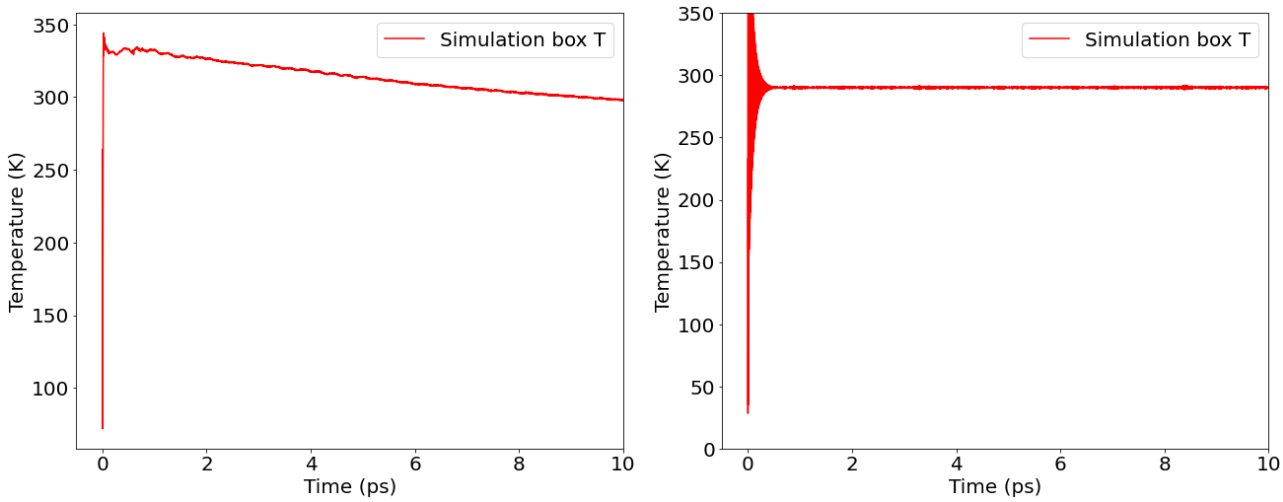

Figure 2.8: The Temperature dependency of time for NVT, left: the simulation without applying *tau_eta*, and right: with *tau_eta* by setting it to 1.

for the box, which is the most reliable integrator and thus the workhorse. This will provide energy and velocity to the atoms in the box.

Chapter 3

Results and Discussion

Sample generation and equilibration in the meaning of the MD simulation, a sample is a file that contains at least all of the essential attributes of all particles in the system. This comprises not just the particle's position and speed, but also the particle type and particle mass. There is a state of least energy for all particles, according to the trough in the LJ potential Figure 2.2. As a result, there is a stagnant condition of equilibrium. Every undisturbed non-equilibrium system achieves equilibrium according to thermodynamic rules. This is known as equilibration. Because a sample might theoretically be in any condition, prior equilibration is critical. Therefore, the equilibration process will occur during the simulation, which may result in inaccurate findings. For the model of this work, it makes sense to look at a sample heated to 293 K. Many of the comparative values for material constants that can be found in the literature are given at this value, which is close to room temperature. In addition, this temperature reflects the problem well.

To put a sample into its condition of equilibrium at this temperature, it is best to first produce a sample at 0 K and then heat it up. The estimated zero point is readily attained because the particle velocities are set to 0. A simulation is run using a homogeneous deformation without taking into account the particle movements generated by the force. In each simulation step, the sample is examined using an incrementally scaled lattice axis-parallel acting deformation matrix. The path of mean potential energy as a result of this may now be reduced [40].

The preceding simulation was carried out in accordance with the principles of a microcanonical ensemble (NVE). This signifies that the total energy E was recorded in addition to the number of particles N and volume V. Because the following phase necessitates a tempera-

ture rise to warm up the sample, an NVE system is always ineffective. Instead, the canonical ensemble (NVT) emerges. The number of particles and volume are also set, but instead of energy, the temperature T is provided by connection to a heat bath. In the simulation, this is accomplished through the use of a thermostat. A thermostat modifies the simulation such that the temperature matches the requirements.

The heating of a simulation box sample using the Nosé-Hoover thermostat implemented in IMD is shown in Figure 3.1. Despite the specification, the temperature oscillates at first, although this effect reduces over time. The variations are fairly consistent from about $25,000$ IMD time units. However, as seen in Figure 3.2, potential energy reacts according to temperature profile. It is thus recommended to run an NVE simulation once the system has reached equilibrium.

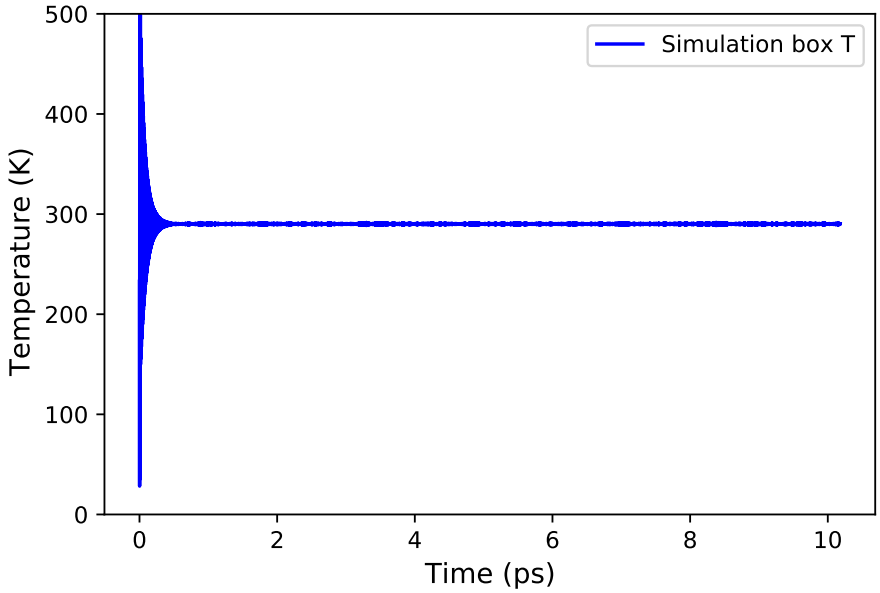

Figure 3.1: The heating process at a specific temperature NVT. As time passes, the variations get smaller.

Due to PBC, samples are frequently cuboid and form a lattice, which largely mimics the features of an indefinitely stretched lattice. However, in the context of this work, spherical forms under gravity are fascinating since they are extremely comparable to powder particles in the SLM process. The easiest technique to produce such a sample is to remove the surrounding particles from a similar lattice segment. It should be emphasized that the sphere is not released until the homogeneous deformation is complete. This is due to the fact that a homogeneous de-

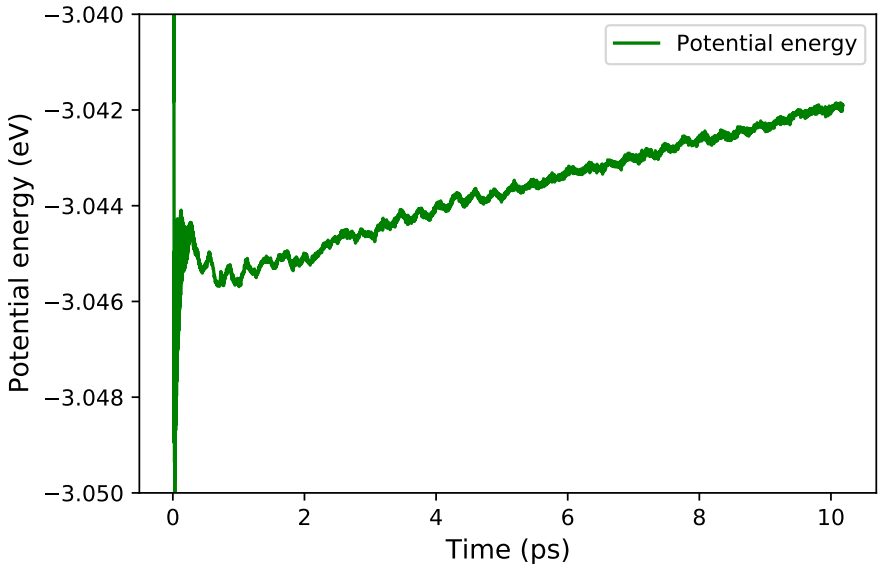

Figure 3.2: The potential energy follows a temperature-proportional path NVT.

formation scales the entire particle system. The radius of the sphere will fluctuate dramatically throughout this operation if it is extremely accurately dimensioned.

In any event, it is critical that the succeeding equilibration processes take place under the effect of gravity and with adequate equilibration time. This causes the balls to sink somewhat and, as a result, shift into its resting position, which matches to the form.

It is often advised that the balls are not be placed immediately within the PBC's field of influence. The PBC might be stopped to prevent such self-interference, but this proved to be advantageous for developing problem related samples. For example, a previously equilibrated simulation box can be replicated numerous times in a sequence to generate a series of spheres. The ground is replicable as long as the original sample has been equilibrated with PBC. The absence of the need to equilibrate the result saves time, especially with bigger samples.

3.1 Studying simulation parameters

In this section, the observation behavior of a row sphere under laser irradiation Figure 2.6. The configuration behaves differently depending on the parameters sphere diameter d, scanning speed v, laser power P, laser beam width σ_{FWHM}, laser offset h, and penetration depth or inverse absorption length $1/\mu$, as will be detailed further below.

3.1.1 Laser Offset

It is the beginning point of the laser emitted from it. The default value is 0, and the laser's orientation is along the z-direction *laser_dir* (001). Because the height (diameter d) varies for each box, the offset h for same diameter balls is diameter of the ball plus ground height, while for different diameter balls in the same simulation box, h is higher than the ball diameter plus ground height. We are investigating the effect of h in different heights in the z-direction. As illustrated in Figure 3.3, the laser is stationary in the middle of the box with only h changing to three values (4 d, 2.1 d, 1.1 d) of the ball's diameter. The laser energy is absorbed in Figure 3.3(c) and all the balls react to the laser power, therefore this $h = 1.1\ d$ is used for the subsequent simulation samples.

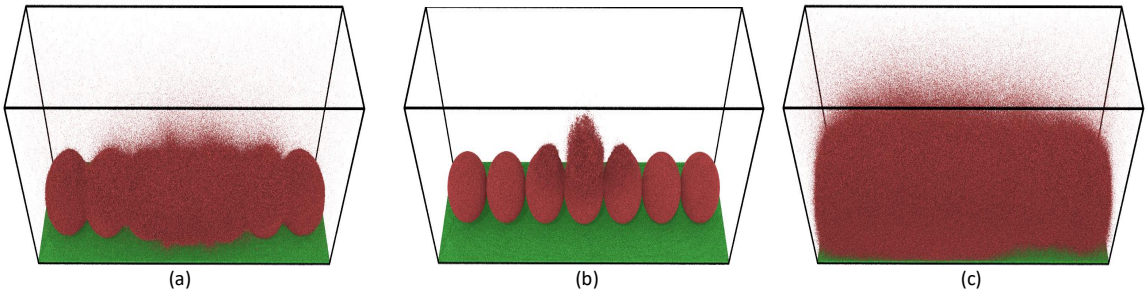

Figure 3.3: (a) $h = 4\ d$, the five center balls absorb more P and begin to evaporate, (b) $h = 2.1\ d$, just three center balls interact with P, (c) $h = 1.1\ d$, when h is close to the sample height, all the balls interact with the P. The remaining simulation parameters are $d = 220$ Å $P = 100$ eV/fs, $\sigma_{FWHM} = 8\ d$, $1/\mu = 80$ Å.

3.1.2 Full Width at Half Maximum

The laser power P used is the total absorbed laser power, not the laser's intensity parameter. By narrowing the σ_{FWHM}, the intensity of the Gaussian beam becomes more concentrated of the laser beam, whereas increasing σ_{FWHM} decreases the intensity of the beam and distributes it over a larger width, which is why when σ_{FWHM} is small, more P is absorbed and the melting percentage increases. As seen in Figure 3.4, this indicates that σ_{FWHM} is expected to behave as in subsection 2.1.1. The result of $\sigma_{FWHM} = 2\ d$ was utilized in the other following simulations.

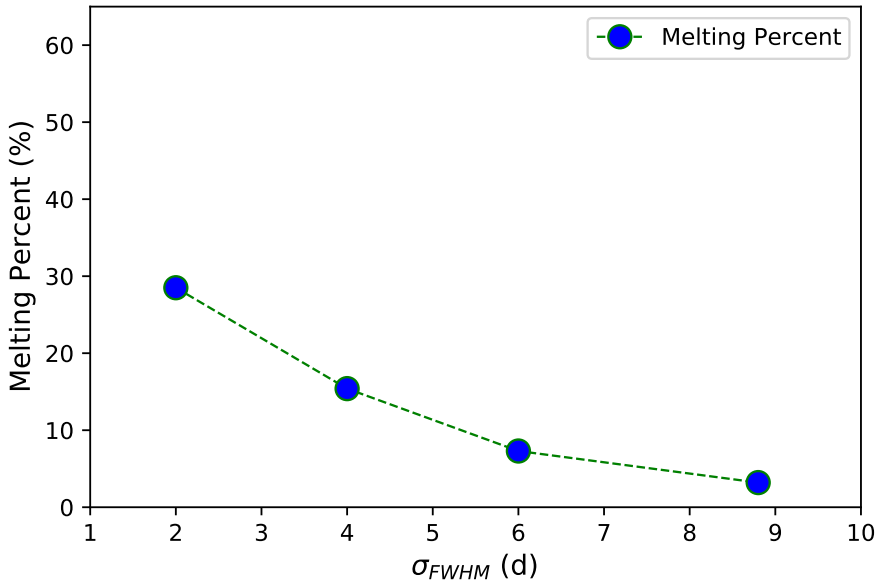

Figure 3.4: By doubling σ_{FWHM} value, the melting percentage in the simulation box decreases, as the Gaussian wave Figure 2.3 becomes broader and wider. The remaining simulation parameters are $d = 55\,\text{Å}$, $P = 100\,\text{eV/fs}$, $v = 5\,\text{Å/fs}$, $h = 1.1\ d$, $1/\mu = 80\,\text{Å}$.

3.1.3 Scanning Speed

The change in scanning speed has a significant impact on the system; for specific simulation box sizes, the effect of the laser scanning speed will have an impact on the absorption of laser energy in the box. Thus, by increasing the laser scanning speed, less energy is absorbed in the system, causing the temperature in the system to be insufficient to melt the Al in the simulation box. Because we regulate the energy disposed in the system by changing the velocity of the laser, the scanning speed of the laser is an essential parameter that has an influence in the system. As shown in Figure 3.5, the laser starts from left to right, and the beam location is out of the box in x-direction to ensure that the Gaussian beam has zero intensity when it reaches the first ball. Another key parameter in the simulation is laser reflectivity, which is set to zero in this scenario to allow for complete absorption $R = 1 - A$, R stands for reflectivity, while A stands for absorptivity, and angle of indecent is zero. The scanning speed in the system is displayed in Figure 3.6 by altering the melting percentage. The system or simulation box is modest in comparison to the scanning speed; the simulation box is approximately 3240 Å, and if $v = 20\,\text{Å/fs}$, the laser will scan the whole simulation box in 162 fs. It is quick enough that the system does not absorb enough P to melt or interact, therefore set the laser velocity to

$5 - 6.5$ Å/fs, which is a suitable pace for the system.

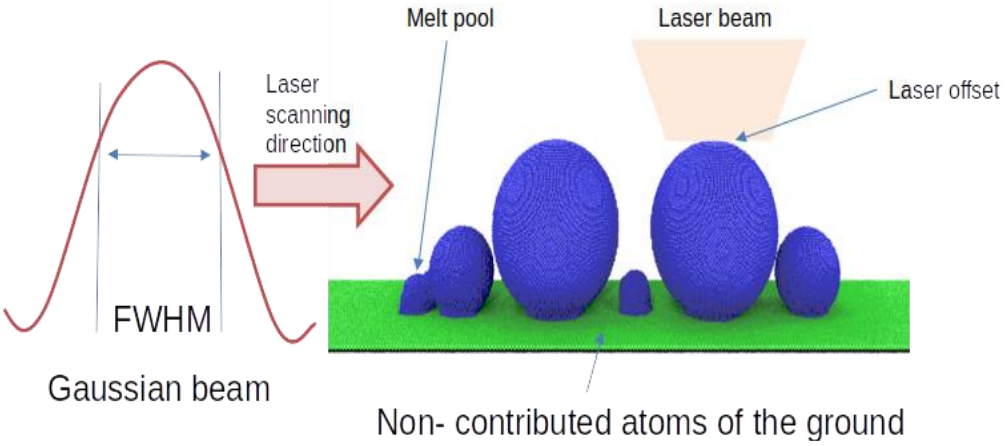

Figure 3.5: Schematic of a laser system in which the laser moves from left to right in a Gaussian profile with velocity v, enters the box, interacts with Al, and melts it as in a melt pool. The offset and the direction of irradiation of the laser are displayed.

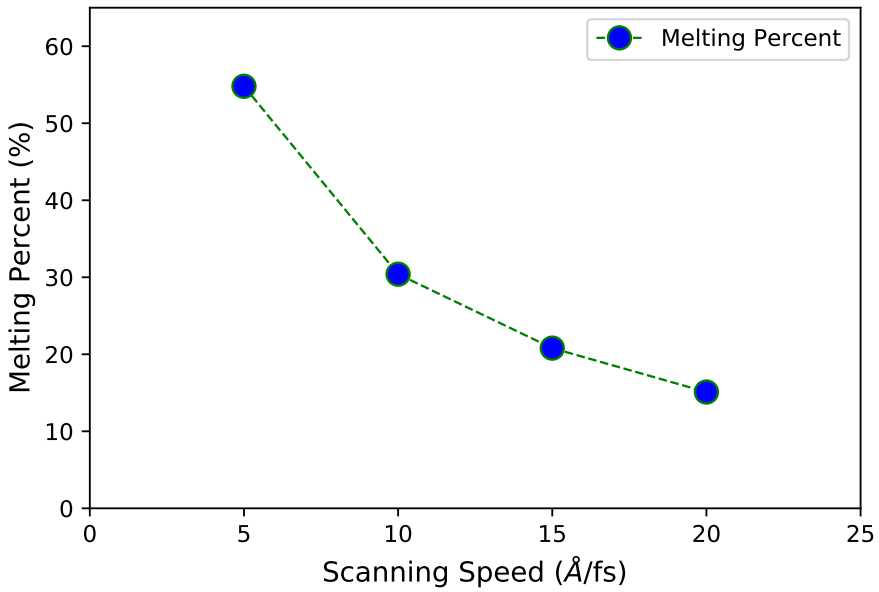

Figure 3.6: Increasing the laser's scanning speed, which has an effect on absorbing energy in the system and causes melting to decrease. The remaining simulation settings are as follows: $d = 220$ Å, $P = 200$ eV/fs, $h = 1.1\ d$, $\sigma_{FWHM} = 2\ d\ 1/\mu = 80$ Å.

3.1.4 Absorption Coefficient

When light absorbs in a homogeneous medium with a certain absorption coefficient, its optical intensity decays as $\exp(-\mu x)$, where x is the propagation distance. It is presumed that a beam's divergence or convergence has no effect on its intensity. For the exponential temperature gradient and scaling laser heating, the absorption length is defined as the inverse of the absorption coefficient. The intensity decays to $1/e \simeq 37\,\%$ of its starting value after that propagation duration. Only $1.8\,\%$ of the initial intensity remains after four absorption lengths. In reality, we cannot modify the μ, but this research attempts to identify the optimal value of the laser since the real value of μ will be too large in this simulation, so instead of using the real value, we use the most re-scale value to the system. This will also result in unreal absorption.

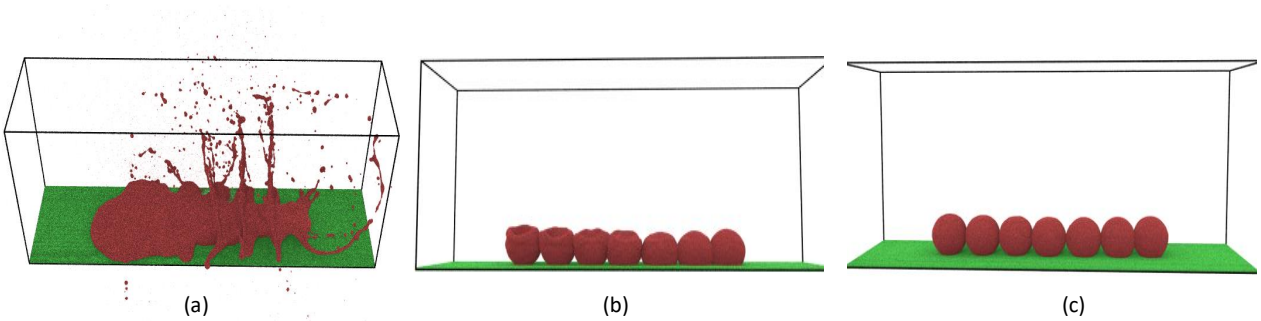

Figure 3.7: (a) $1/\mu = 66\,\text{Å}$, the laser energy has been absorbed, melted, and expelled, (b) $1/\mu = 88\,\text{Å}$, absorption establish has occurred, but only the upper portion of the Al balls has melted, while (c) $1/\mu = 110\,\text{Å}$, absorption establish has occurred, but there was little absorption because the $1/\mu$ became so low that the energy of the laser was insufficient to melt the Al; in this situation, the laser power should be increased. The following are the remaining simulation settings: $d = 220\,\text{Å}$, $P = 200\,\text{eV/fs}$, $v = 5\,\text{Å/fs}$, $h = 1.1\ d$, $\sigma_{FWHM} = 2\ d$.

Figure 3.7 shows the considerable influence of penetration depth. To investigate μ further, we increased the $1/\mu$ while keeping the laser power constant at $P = 200\,\text{eV/fs}$, since we assumed that absorption would cease at that level, as shown in Figure 3.8. The $1/\mu = 55\,\text{Å}$ evaporated and exploded the balls, thus it became the minimum for value $1/\mu$ as illustrated in Figure 3.10.

The effect of $1/\mu = 132\,\text{Å}$, at power $= 2000\,\text{eV/fs}$ is equivalent to the effect of $1/\mu = 125\,\text{Å}$, at power $= 1600\,\text{eV/fs}$, which indicates that altering $1/\mu$ by $7.45\,\text{Å}$ has the same impact as increasing power by $400\,\text{eV/fs}$, as shown in Figure 3.9. As a result, by concentrating on the range of $65-75\,\text{Å}$ of the $1/\mu$ to see the change in temperature in the system, as shown in

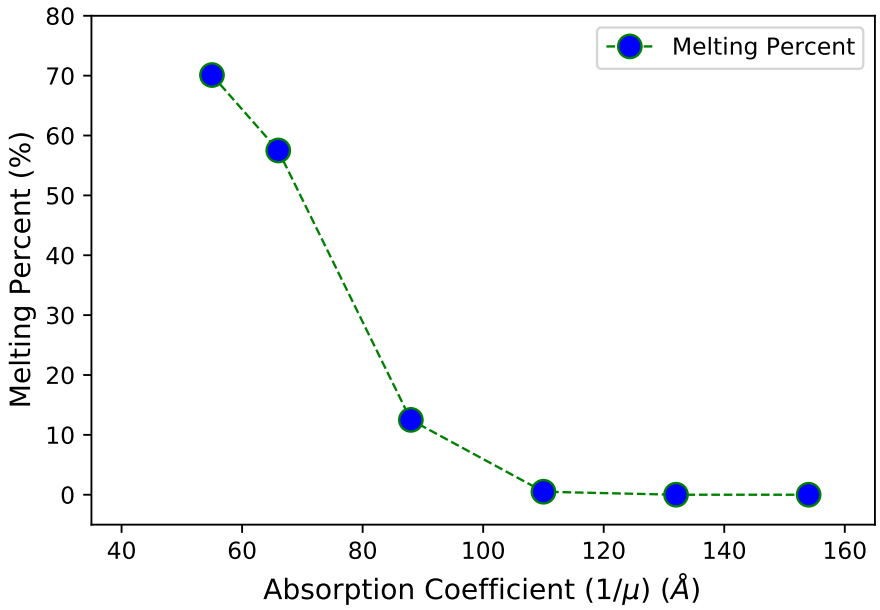

Figure 3.8: The laser's absorption coefficient, which decreases the value of μ by increasing to near the diameter of Al balls, and decrease the melting percentage. The remaining simulation variables are as described in the following: $d = 220\,\text{Å}$, $P = 200\,\text{eV/fs}$, $v = 12.5\,\text{Å/fs}$, $h = 1.1\ d$, $\sigma_{FWHM} = 2\ d$.

Figure 3.11, the impact is effective for minor changes in the $1/\mu$, and selecting $1/\mu$ to be 70 Å.

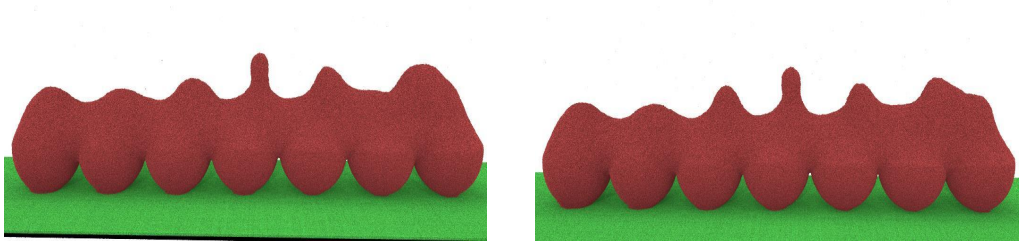

Figure 3.9: Left: the value of $1/\mu = 132\,\text{Å}$, and the $P = 2000\,\text{eV/fs}$, right: $1/\mu = 125\,\text{Å}$, at 1600 eV/fs The two situations are strikingly identical, with just a little change in the last ball on the right in both pictures. The remaining simulation variables are as described in the following: $d = 440\,\text{Å}$, $v = 6.25\,\text{Å/fs}$, $\sigma_{FWHM} = 2\ d$.

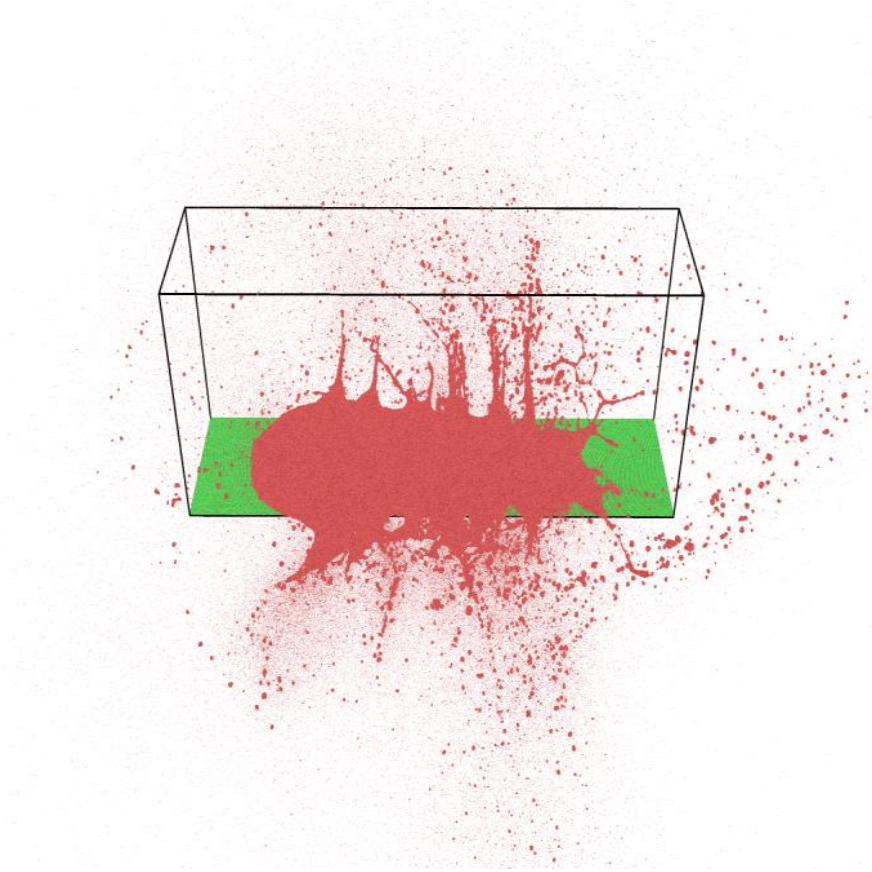

Figure 3.10: The effect of $1/\mu = 55\,\text{Å}$ showed how the balls melted, burst, and splashed all over the box, and we don't want this to happen to the balls, as a result, we do not utilize less. There is no PBC for the box here. The following are the remaining simulation settings: $d = 220\,\text{Å}$, $P = 200\,\text{eV/fs}$, $v = 5\,\text{Å/fs}$, $h = 1.1\ d$, $\sigma_{FWHM} = 2\ d$.

3.1.5 Laser Power

The laser beam Power is another aspect in the simulation that has a significant influence on the system; it is self-evident that the laser power controls the energy deposited in the system. Changing the laser intensity to get the desired temperature for melting the Al in the box, which is 933.7 K [41]. Volume of laser atoms per particle (inverse density), it is necessary to establish how much of the spatial energy density is contained in each atom. As previously stated, approximations are occasionally utilized for this model, making it very hard to directly convert simulation data to actual measurement data via a pure measurement variable conversion. A mostly qualitative comparison of the observations with the outcomes of experiments is proposed to validate the model. The impact of the laser power should be investigated before adjusting

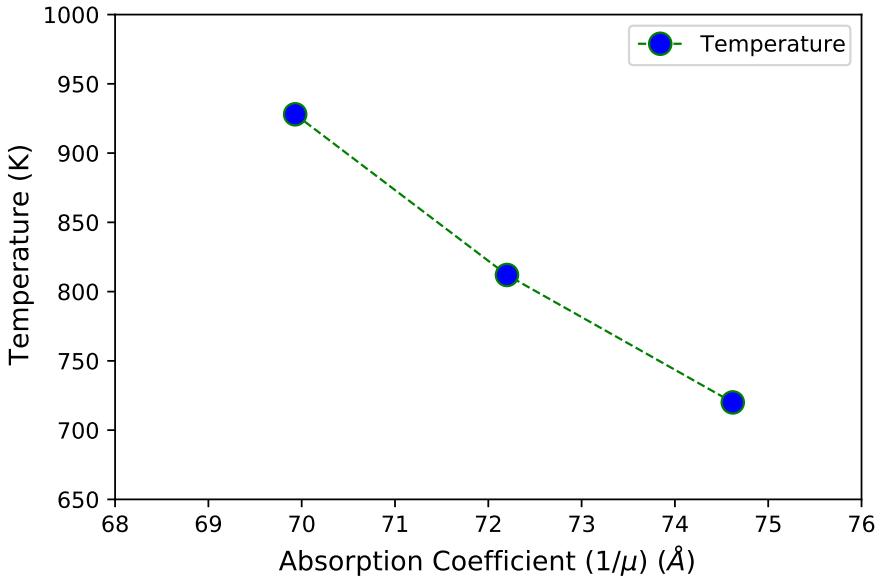

Figure 3.11: Changing the value of $1/\mu$ to 69.63 Å, 72.2 Å, 74.62 Å to observe how it affects the temperature in the box by setting the other parameters to $d = 440$ Å,$P = 200$ eV/fs, $v = 6.25$ Å/fs, $\sigma_{FWHM} = 880$ Å, $h = 460$ Å.

the other parameters. Various research are now being simulated in order to create reference simulations on which to base future research. At this rate, the preliminary objective is to assign a meltability to each performance. The temperature was measured for each laser power value. Increasing the power clearly raises the temperature of the system, and increasing the $1/\mu$ raises it even more. As seen in Figure 3.12 for $1/\mu = 70$ Å and 74.62 Å the power effect in the simulation box, respectively.

The system reaches the melting temperature of the Al at $P = 100$ eV/fs, however as seen in the left Figure 3.13, only the upper section of the balls have melted. This suggests that just the upper section of the ball absorbed the laser power and the ball itself did not reach a high enough temperature to melt. However, when $P = 500$ eV/fs, the temperature rises to approximately 2500 K and the balls absorbed enough energy from the laser to begin evaporate.

3.1.6 Simulations with added Argon gas

Argon is a noble gas with a high degree of inertness (i.e. it is chemically relatively unreactive). Physically, it is a simple chemical since it is a mono-atomic as a gas or fluid (no covalent bonds that form molecules) and apolar. As a result, it can be represented as a neutral molecule. In

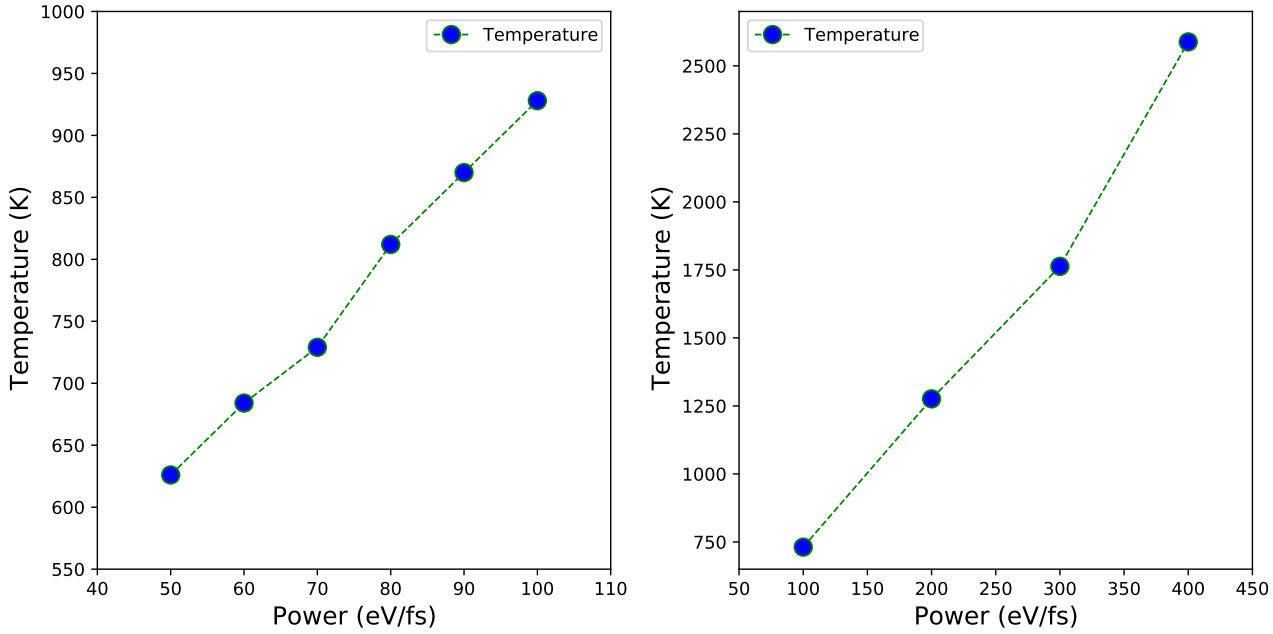

Figure 3.12: The temperature increase by increasing power for right $1/\mu = 70\,\text{Å}$, and left $1/\mu = 74.62\,\text{Å}$. We observe that the growth is linear, and that increased μ further increases the temperature. The remaining simulation variables are as follows: $d = 440\,\text{Å}$, $v = 6.25\,\text{Å/fs}$, $\sigma_{FWHM} = 880\,\text{Å}$, $h = 460\,\text{Å}$.

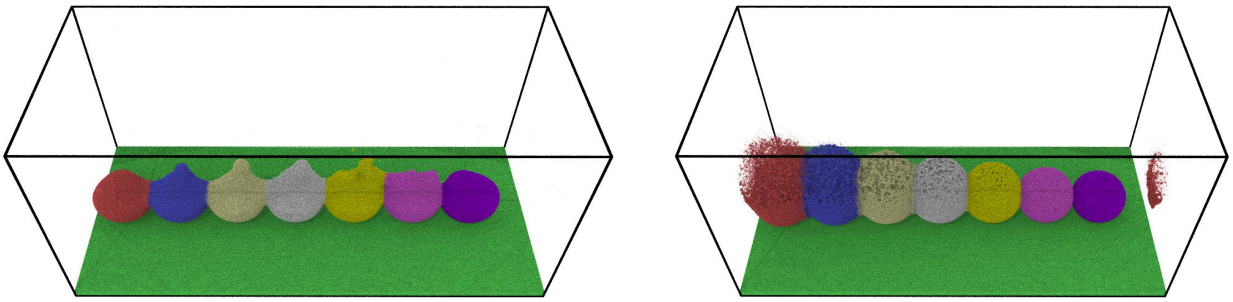

Figure 3.13: Left: $P = 100\,\text{eV/fs}$, the upper layer of balls has been melted. Right: $P = 500\,\text{eV/fs}$, the balls begin to evaporate rather than melt. By keeping these parameters constant: $d = 400\,\text{Å}$, $1/\mu = 80\,\text{Å}$, $v = 5\,\text{Å/fs}$, $\sigma_{FWHM} = 1.6\ d$, $h = 550\,\text{Å}$.

terms of the force field, the two important force field terms in Ar are Pauli-repulsion (which prevents atoms from overlapping) and London-dispersion (induced dipole-dipole interactions), which are characterized by a LJ potential. Ar is utilized in laser powder bed fusion in the AM process because it generates the ideal atmosphere for the process. Building components in a controlled environment while minimizing the entry of any potential contaminants is a key

difficulty in metal AM. Inerting is also essential for the efficient management of flammable dust generated by the powder metal and printing processes. The elimination of projections and fumes created at the meltpool is a crucial cause for a steady gas flow above the powder bed. Without it, the fumes would interfere with the laser and the projections would cause material problems. Typically, AM takes place in an open environment, behind a protective gas, or under a liquid cover. Simulations, on the other hand, usually take place in a vacuum. This may result in improved spraying of the heated substance. Adding a model gas may operate as a repellent, absorbing the momentum of the heated droplets and cooling them so that they fall back to the formed surface.

The objective now is to uniformly fill the space between spheres of variable size with Ar. A thermodynamic strategy would be to construct a plane of Ar particles above the spheres, then heat the system via NVT until the Ar has filled the free volume. The method has been proved to function well, but it is rather slow and wastes a lot of computing time because the sample must then be cooled and the entire system must be equilibrated.

By adding a layer of the Ar gas atoms to the simulation box, and after equilibrating the system, the Ar atom will fill the vacant space in the simulation box, as shown in Figure 3.14.

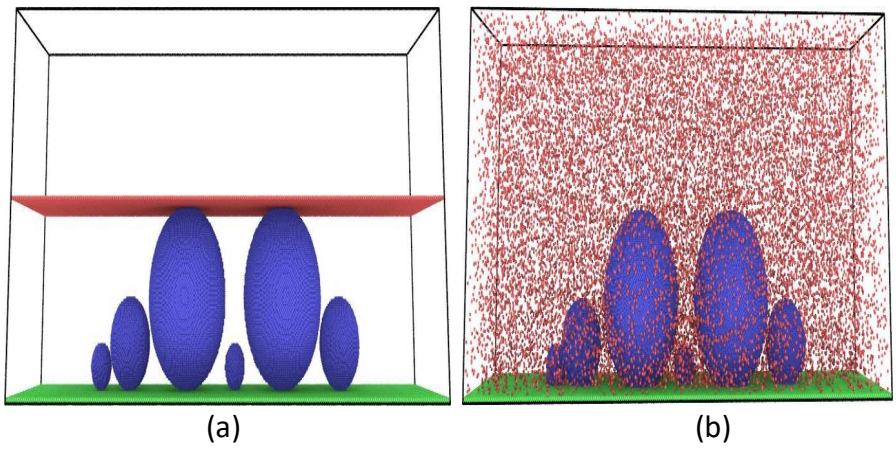

Figure 3.14: (a) Before adding an Ar layer to the simulation box, the layer is 5 Å thickness which contain only one layer of Ar atoms, and (b) after equilibrating the sample to room temperature with NVT will filled the box with Ar (red), Al (blue), ground (green) atoms.

3.1.7 Impact of the Argon

The simulation filled with Ar atoms and after equilibrating the box and running laser on it, as shown in Figure 3.15 (a) the surface of the Al spheres gets roughness and the original arrangement of spheres remains more visible because the gas cools the Al. However, in Figure 3.15(b) where there is no Ar in the box, the spheres melt and fuse together.

The fraction of material in the sample that has melted after the simulation defines this. For this CNA is utilized as a decision criteria in visualization tool Ovito. A CNA is a tool used to recognize and name lattice structures. Thus, if an atom in Al known to have a FCC lattice structure is identified as part of another structure, it must in this context be molten Al and other structures that convert the Al to relatively small numbers are ignored. Experience has proven that this is typically highly reliable, but it should not be overlooked. To see the effect of the Ar in the box, we removed the Ar atoms to one layer, which is equivalent to 5.9 % of the whole atoms in the box, and also lower the scanning speed to guarantee proper absorption. The impact of varied Ar gas concentrations can be observed in Figure 3.16, where the amount of Ar has an effect on making Al melt nearly 99 % of the time without causing the Al balls to burst or evaporate.

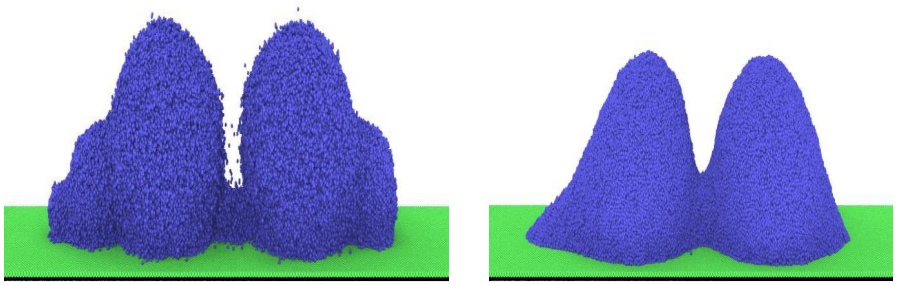

Figure 3.15: (a) With Ar, which is not depicted here, to see how Al will behave or melt if there is no room to expand due to the Ar atoms and interaction of the two types of atoms with different masses, and (b) without or without Ar. Al (blue), ground (green) atoms, the other parameters are $P = 1600\,\text{eV/fs}$, $1/\mu = 121\,\text{Å}$, $v = 6.25\,\text{Å/fs}$, $\sigma_{FWHM} = 880\,\text{Å}$, $h = 165\,\text{Å}$.

When compared to the number of atoms in the simulation box for the one with Ar, the

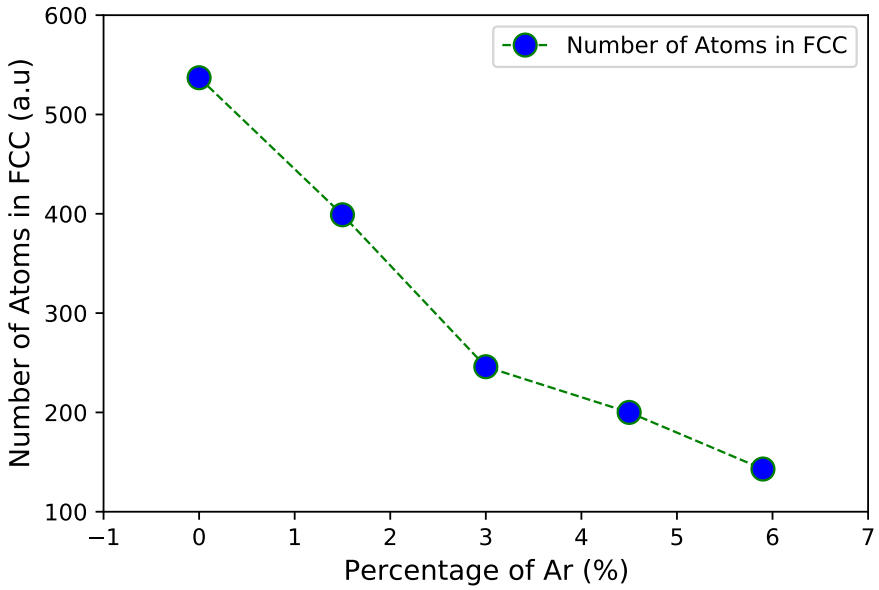

Figure 3.16: The fraction of Al that has not melted in the FCC structure as compared to the the percentage of Ar in simulated box. The following parameters were used: 800 eV/fs, $v = 1.1$ Å/fs, $\sigma_{FWHM} = 880$ Å, $h = 165$ Å, $1/\mu = 69.93$ Å.

number of Al in FCC structure not melted is 143 atoms, while the one without Ar, Al not melt is 537 atoms, which is on the order of 5 times the number of atoms in the simulation box for the one with Ar, indicating less Al melt in the simulation box. In Figure 3.17 a.1 is just Ar atoms (Al atoms have been removed), meaning that there are not many Ar atoms in the melted Al, Figure 3.17 a.2 and b.1 are only Al atoms (after removing the Ar atoms in Figure 3.17 a.2), how the Al melted, Figure 3.17 a.3 and b.2 the FCC structure of Al.

As a consequence, 5.9 % of the Ar in the box is a better proportion to determine what power would suitably melt all Al or the least power for all Al atom melt and taken range of power to examine the effect as shown in Figure 3.18, and shown how much of the Al's FCC structure has melted by each laser power using CNA as shown in Figure 3.19.

3.2 Discussion

In this section, we will discuss the temperature of the various types of atoms in the simulation, as well as the energy absorbed by the system. As shown in Figure 3.18 and Figure 3.19, the first sample which has $850.395 \times 202.475 \times 323.96$ Å dimension and $(357, 614)$ atoms, the Al

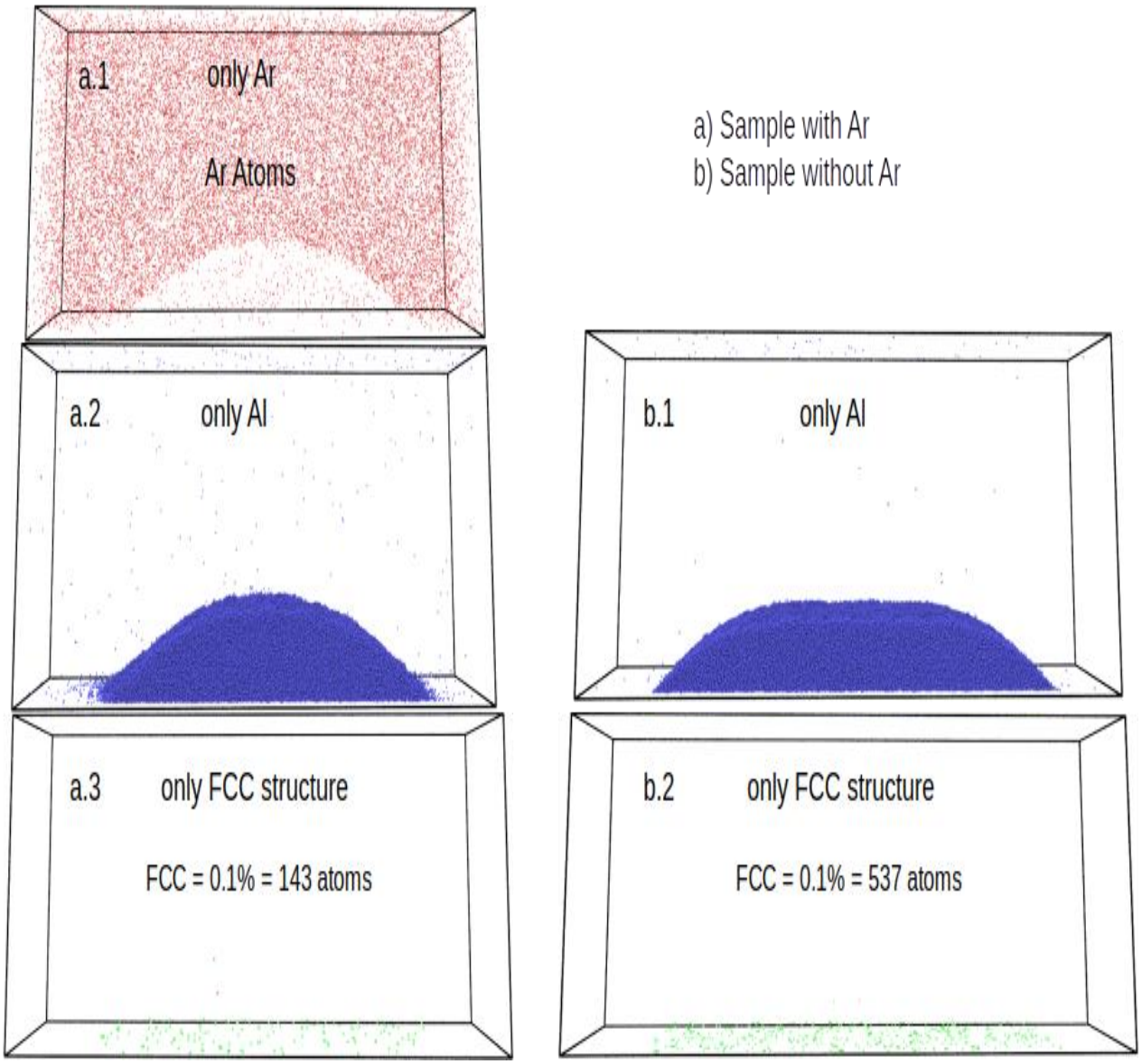

Figure 3.17: (a) With Ar gas, (b) without Ar gas in simulation box. The parameters are $P = 800\,\mathrm{eV/fs}$, $v = 1.1\,\mathrm{Å/fs}$, $\sigma_{FWHM} = 880\,\mathrm{Å}$, $h = 165\,\mathrm{Å}$, $1/\mu = 69.93\,\mathrm{Å}$.

atoms are virtually melted with few defects at a power equivalent to 800 eV/fs, so we begin by analyzing the temperature and energy of each Al, Ar and the ground atoms. As shown in Figure 3.20 left, the ground temperature is zero (green), indicating that the NVT has no effect on increasing the ground temperature, and the Al (blue) are nearly at room temperature close to 293 K, but the Ar temperature is too high approximately 2100 K at the start of the simulation,

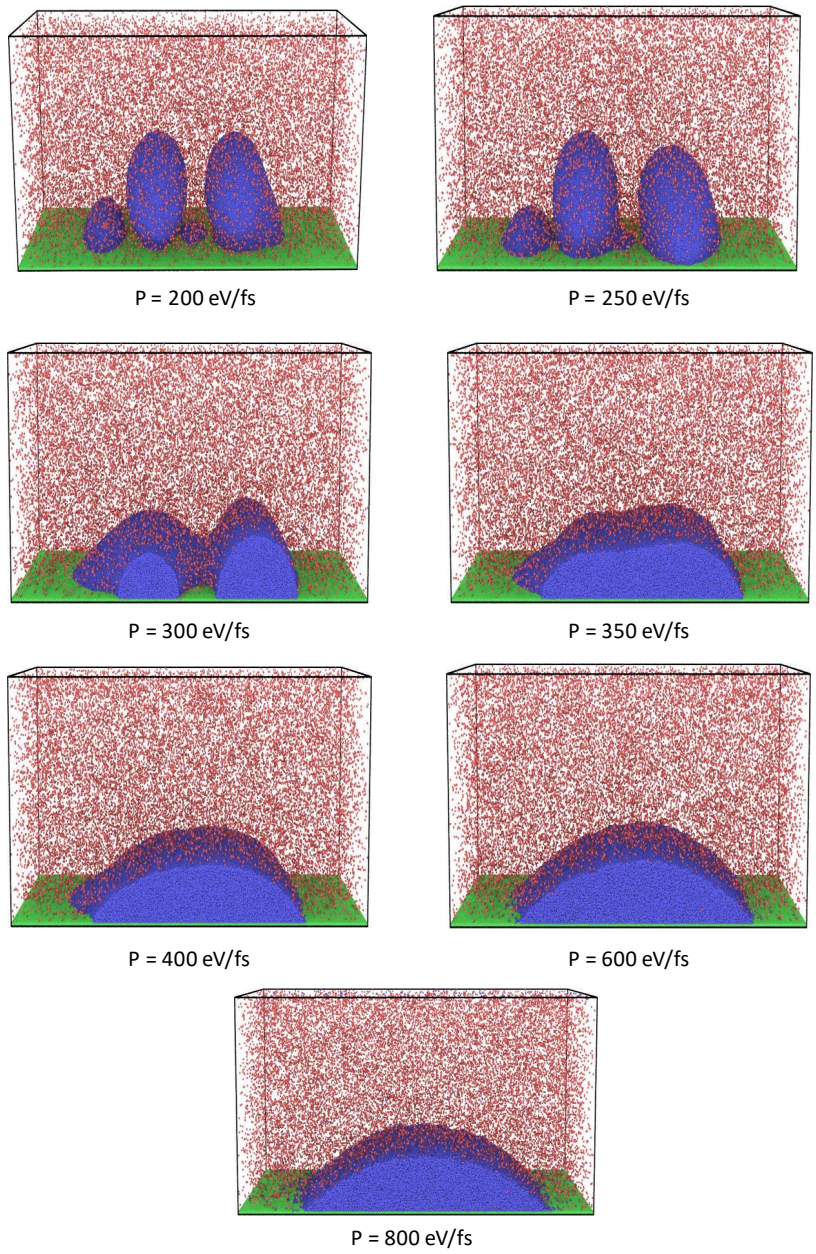

Figure 3.18: Changing laser power from 200 eV/fs to 800 eV/fs, after the laser power is raised while the scanning speed $v = 1.1$ Å/fs, penetration depth $1/\mu = 69.93$ Å, and beam width $\sigma_{FWHM} = 880$ Å, $h = 165$ Å remain constant. The Al configuration begins to melt at $P = 250$ eV/fs, partial fusion occurs at $P = 300$ eV/fs, and total fusion happens above $P = 350$ eV/fs.

but begins to decrease to approximately 1500 K at the end of the simulation's running time. We can also examine the overall energy of each type of atom.

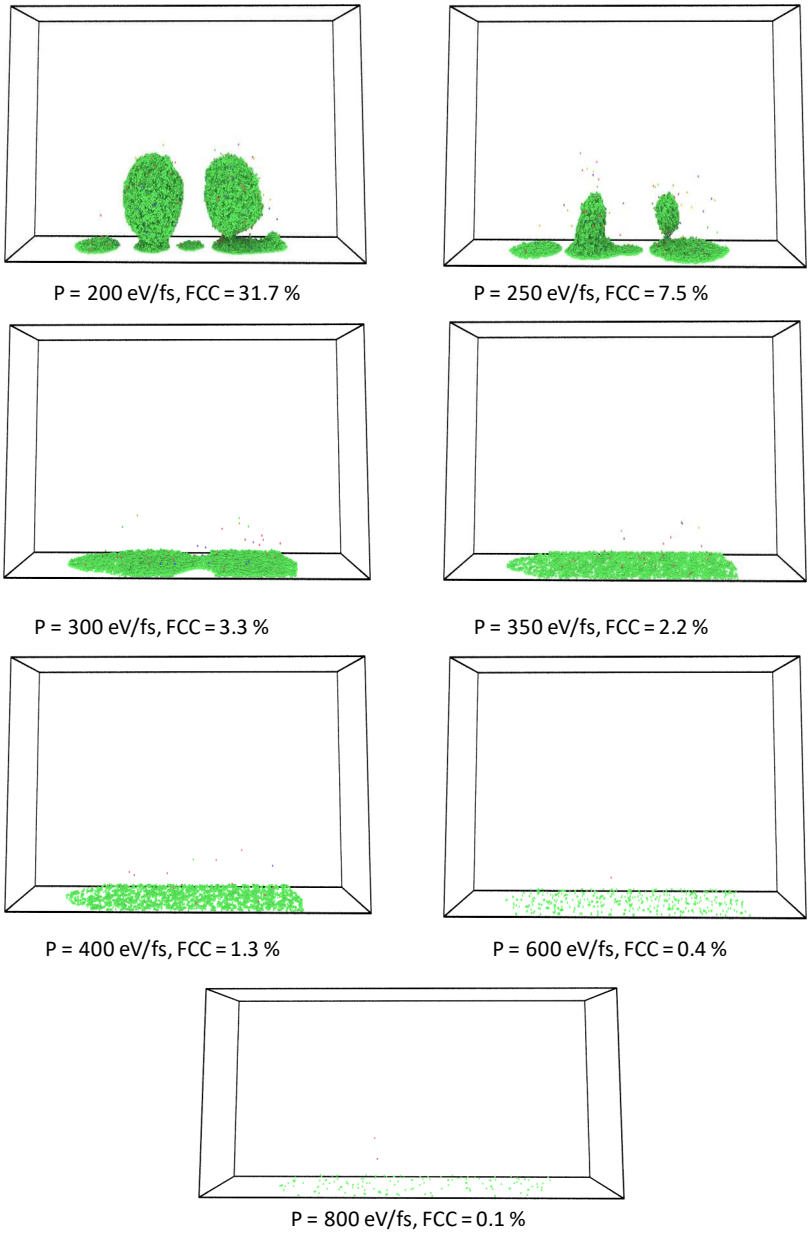

Figure 3.19: Almost all of the Al has melted at $P = 800\,\mathrm{eV/fs}$, and 31.7 % has not melted at $P = 200\,\mathrm{eV/fs}$, and with these parameters $v = 1.1\,\mathrm{Å/fs}$, $\sigma_{FWHM} = 880\,\mathrm{Å}$, $h = 165\,\mathrm{Å}$, $1/\mu = 69.93\,\mathrm{Å}$.

The layer of Ar in box which added to box to be modified later to fill the empty space in the simulation box as seen in Figure 3.14 (a) before equilibrating, but at Figure 3.14 (b) after equilibrating, and added potential and temperature to it, its gain kinetic energy, because of repulsive energy, which increase the temperature of the Ar atoms higher than it should be,

because the distance between the Ar atoms roughly 4.045 Å equal to lattice constant of Al before the equilibrating. Though the high temperature of the Ar atoms has no influence on the ability of the Al atoms to reach room temperature. If we continue the simulation for a longer period of time, the temperature of the Ar atoms will most likely fall to room temperature. On the right Figure 3.20, the energy of the individual atoms in the box is indicated, with the Ar atoms having the highest energy due to their high kinetic energy.

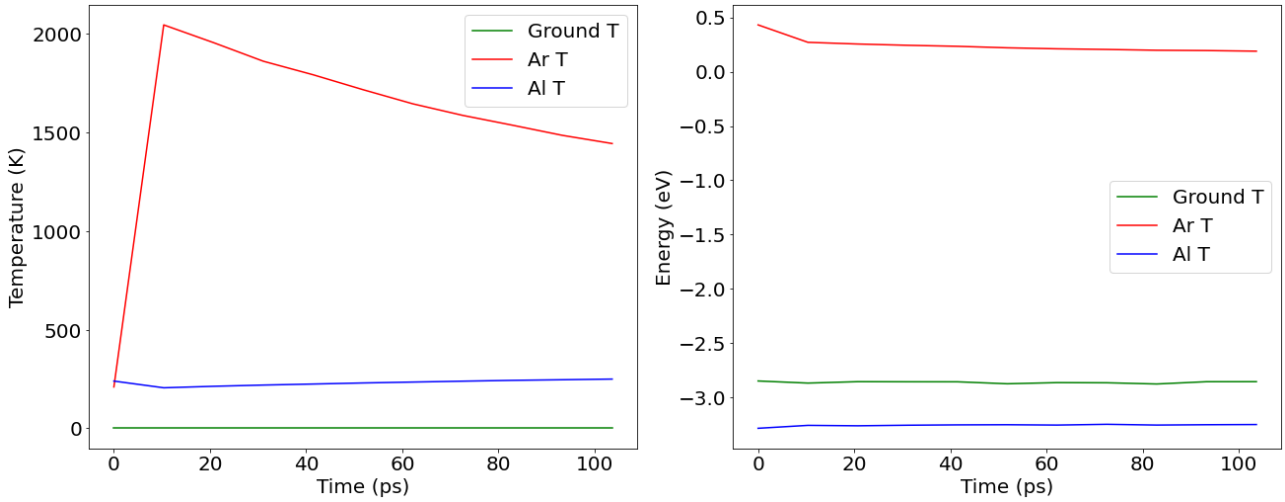

Figure 3.20: The temperature with time steps, when Ar (red line) has risen to roughly 2100 K, and Al (blue line) temperature has reached 293 K. When equilibrated by NVT, the energy of three types of atoms in the simulation box.

After bringing the system to room temperature for the Al, we use a laser with an ensemble NVE for a box with or without Ar, as shown in Figure 3.17. The temperature of Ar has climbed to 17 500 K in the sample containing Ar atoms due to absorbing the laser power from the start of the simulation until the laser leaves simulation box after near to 32 ps, which at that point it begins to decrease and reaches the temperature of Al. As shown in Figure 3.21, the temperature of Al and ground has absorbed energy from the laser power to Al approximately 3000 K and ground just about 1500 K, and stayed stable till 250 ps, because the system is a closed box, the temperature should be kept constant.

When we examine the sample without Ar, we can observe how big of a difference it makes in the temperature required to melt the Al. The temperature of the ground is about the same as that of Ar and Al approximately 2250 K, as indicated in Figure 3.22. We removed the Ar temperature from the panel in Figure 3.23 to concentrate on Al and ground temperature. The

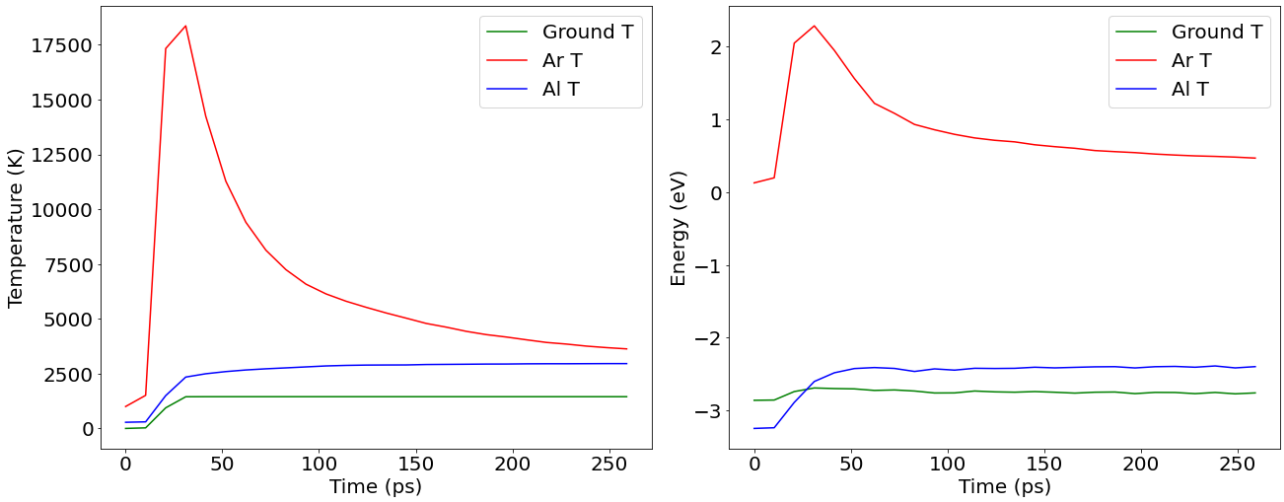

Figure 3.21: Left: we observe how the Ar atoms interact with the laser from the start to the end of the simulation, where the temperature increases to more than 17 500 K when the laser enters the box and decreases when the laser leaves the box and begins equilibrium. For Al to reach around 3000 K and become stabilised till the end of the simulation, right: energy of the box, where the energy of Ar is large due to the kinetic energy of Ar atoms, but Al has little kinetic energy, so only pick up slight total energy from the first ps. The parameters are $P = 800\,\text{eV/fs}$, $v = 1.1\,\text{Å/fs}$, $\sigma_{FWHM} = 880\,\text{Å}$, $h = 165\,\text{Å}$, $1/\mu = 69.93\,\text{Å}$.

difference is that the number of Al in FCC melts is larger, allowing for fewer system faults. Also, the energy of Al is greater than that of Figure 3.22.

Based on the results above, the parameters and size of the simulation box give promising and really good results for doing further simulation on lager size box as $4859.4 \times 1214.85 \times 1943.76$ Å and $(56, 951, 349)$ atoms, after adjusting the parameters to lager sample and applying to different laser power 35 200 and 24 200 eV/fs. We ran across a problem in which the larger ball in the box burst and the other balls melted; after analyzing, we learned that the error was the Equation 2.32 in the laser file, which applies laser parameters to the system. The fault was the value of the z or the depth of the value is laser offset (h) $(h - z)$, where the laser intensity or laser power begin to decline after the laser h by $1/e$ for a value of $1/\mu$. In the case of the small sample 1 of (40 Å, 80 Å, 160 Å), the $1/\mu = 69.93$ Å and the h of the laser was at 165 Å, so the laser power was decaying by $1/\mu = 69.93$ Å for the two smaller sizes by $(1.7\ \&\ 1.2 \cdot 1/e)$ until the absorbing by the balls took place, except for the lager one 160 Å. And thus causes the absorbing for the different size balls inside the box to differ, since the absorption of the laser

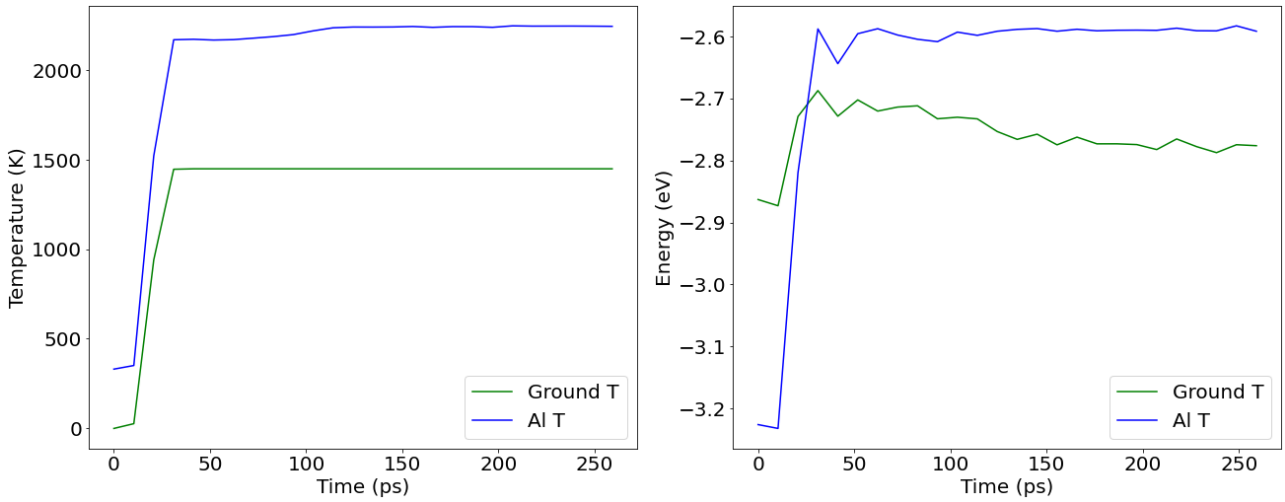

Figure 3.22: Left: here we are looking at the temperatures of the box without Ar, where the ground temperature is about 1500 K, which is the same as with Ar in the box also as in Figure 3.23, but the Al temperature has become around 2250 K, which is nearly 750 K different from Al in Figure 3.21 or Figure 3.23, which makes effect the melt of Al as mentioned previously, right: energies in the box. The parameters are $P = 800\,\mathrm{eV/fs}$, $v = 1.1\,\text{Å/fs}$, $\sigma_{FWHM} = 880\,\text{Å}$, $h = 165\,\text{Å}$, $1/\mu = 69.93\,\text{Å}$.

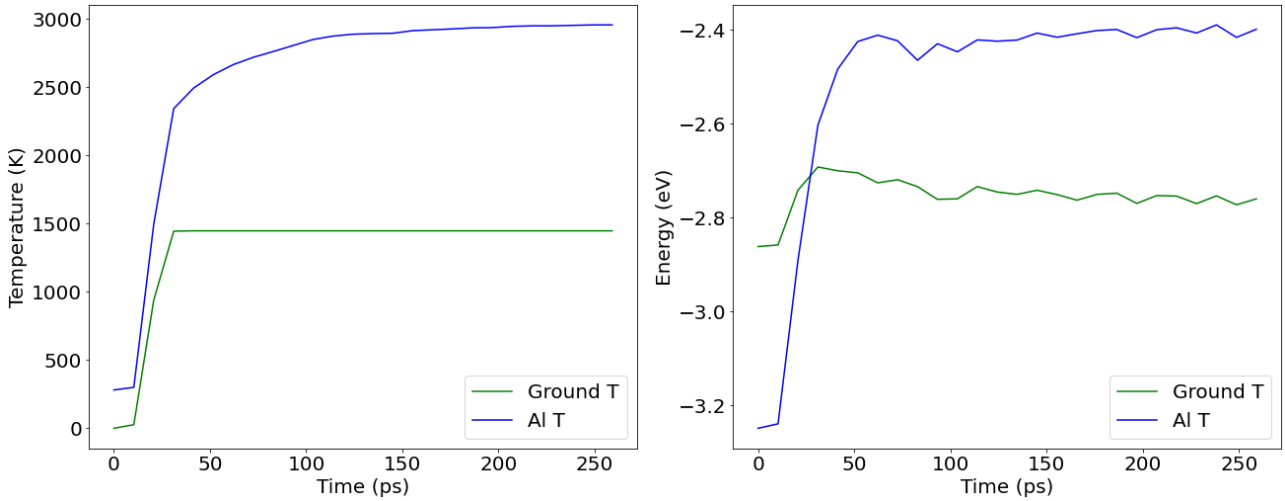

Figure 3.23: This is the same graph as in Figure 3.21, but only the Ar temperature has been removed to provide a closer look at the temperature of the Al and ground. The parameters are $P = 800\,\mathrm{eV/fs}$, $v = 1.1\,\text{Å/fs}$, $\sigma_{FWHM} = 880\,\text{Å}$, $h = 165\,\text{Å}$, $1/\mu = 69.93\,\text{Å}$.

power has been lowered to $1.7 \cdot 1/e$ times for the size of 40 Å. However, in the case of the large sample 2 (220 Å, 440 Å, 880 Å), the h was set to 880 Å and the $1/\mu = 384.61$ Å, the same rate

the laser power drops, and higher number of atoms in the system, which make more interact with laser power, resulting in increase all values of parameters, although the laser power is possibly too high. To view the final result, further adjustments must be made, as well as the simulation time.

The μ should decay by $1/e$ when it enters the Al balls, not before, and this is the flaw that causes not all sizes of Al to have the same laser intensity. So it indicates that the Equation 2.32 works properly when the Al particles are the same size and have the same h of the laser to ensure that the decay of the laser power is the same for all balls when it is absorbed by the Al atoms, which is why the effect is more noticeable in the case of large sample 2. The explosion of the larger ball at two different temperatures is depicted in Figure 3.24, while the temperature and energy of the system are depicted in Figure 3.25 and Figure 3.26. At Figure 3.27, run the same size simulation box but without the Ar for 24 ps, since the temperature has riced to practically the same temperature as the $P = 24\,200\,\mathrm{eV/fs}$ with Ar, which means we will see the same results, and also as the sample 1. By observing the variations in Figure 3.24 (d) and (f).

When we compare the two figures, Figure 3.21 and Figure 3.25, we can observe that the temperature and energy have about equalized. If we look closely at the Al temperature after removing the Ar temperature from the Figure 3.28, we can see that it reached 2500 K and began to cool down to around 2000 K, and we can also see that the ground temperature has rapidly dropped to zero, at the period of time that laser left the box, and no more absorption taking place for the ground atoms, so the lost energy to the system, and started to cool down, or possibly because running the file multiple times causes the ground temperature to drop as well, as we see in both cases. As we can see in Figure 3.26, there is a sharp increase in temperature as well as energy, which could be due to the high power of the laser and interacting between the atoms of the large balls with high velocity, which increases instantaneously temperature for ps and then returns to normal state, or a fault in the simulation.

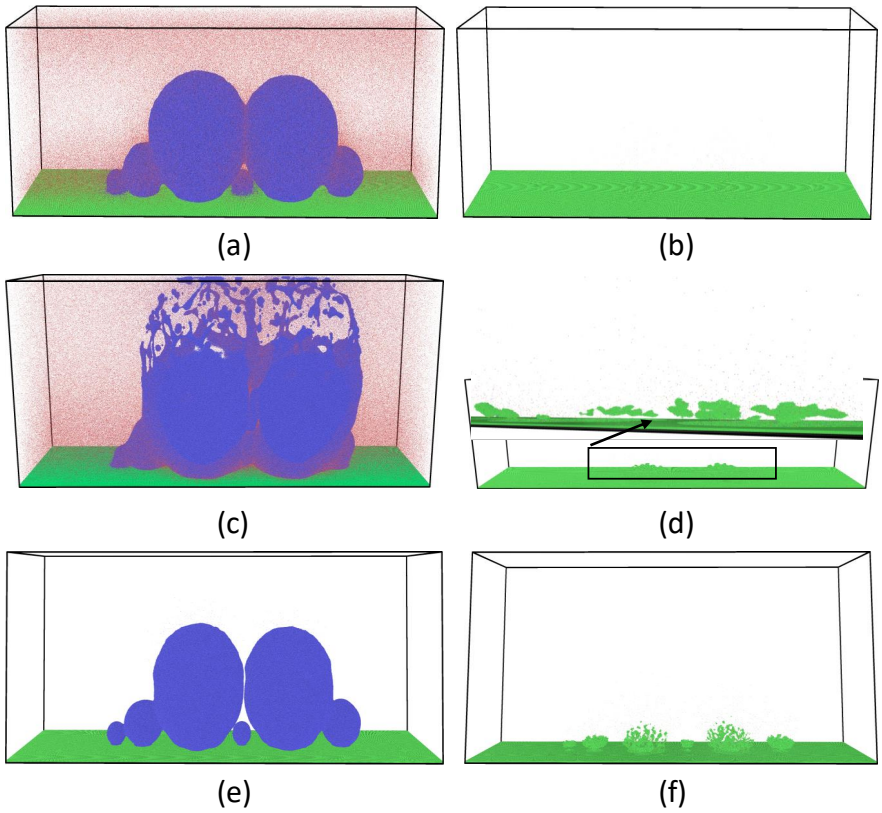

Figure 3.24: (a) and (b), the laser power is 35 200 eV/fs at 21 ps, (a) the Al structure, (b) the only FCC structure of the Al, which means there is no FCC structure remaining except the ground. (c) and (d), $P = 24\,200$ eV/fs at 82 ps, (c) we observe the upper portion of the lager balls exposed, and (d) even after 82 ps the FCC structure of the Al, the outer lower section of the big balls are not melted. (e) and (f), $P = 24\,200$ eV/fs at 24 ps where there are no Ar atoms, (e) we don't observe much Al has melted, but (f) just the outer lower part of the balls remain in the FCC structure like at (d). The parameters are as follows: $d = 220$ Å, 440 Å, 880 Å, $v = 6.25$ Å/fs, $\sigma_{FWHM} = 880$ Å, $h = 900$ Å, $1/\mu = 384.61$ Å.

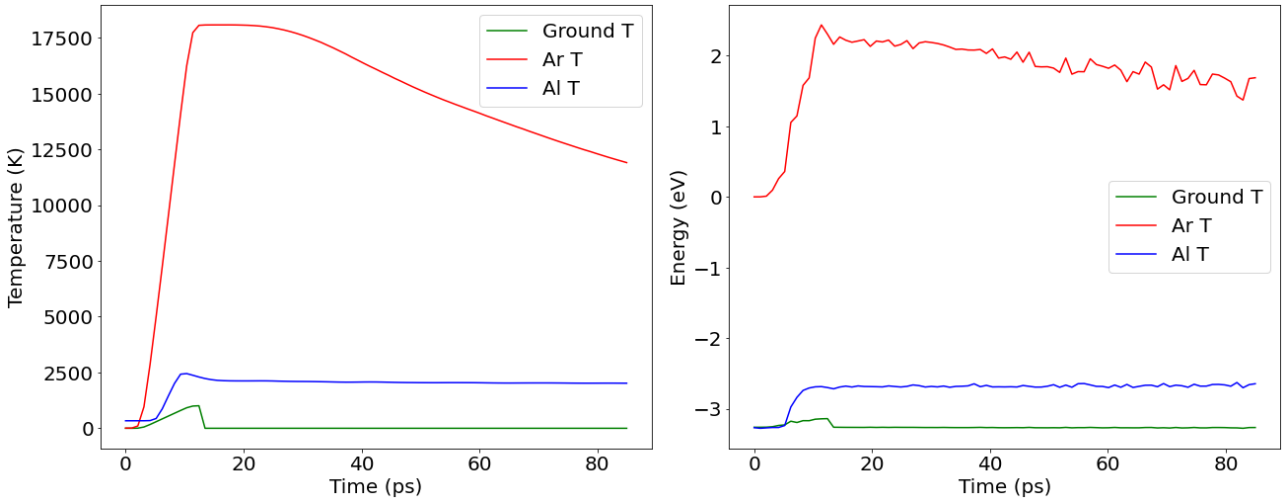

Figure 3.25: We see here for 82 ps that the big sample behaves like the small sample as in Figure 3.21, which means that the parameters are well defined from small to bigger sample, but the only thing we noticed here is that the ground temperature goes to zero, which could be due to multiple running simulations having this effect. The following are the parameters: $P = 24\,200\,\text{eV/fs}$, $v = 6.25\,\text{Å/fs}$, $\sigma_{FWHM} = 880\,\text{Å}$, $h = 900\,\text{Å}$, $1/\mu = 384.61\,\text{Å}$.

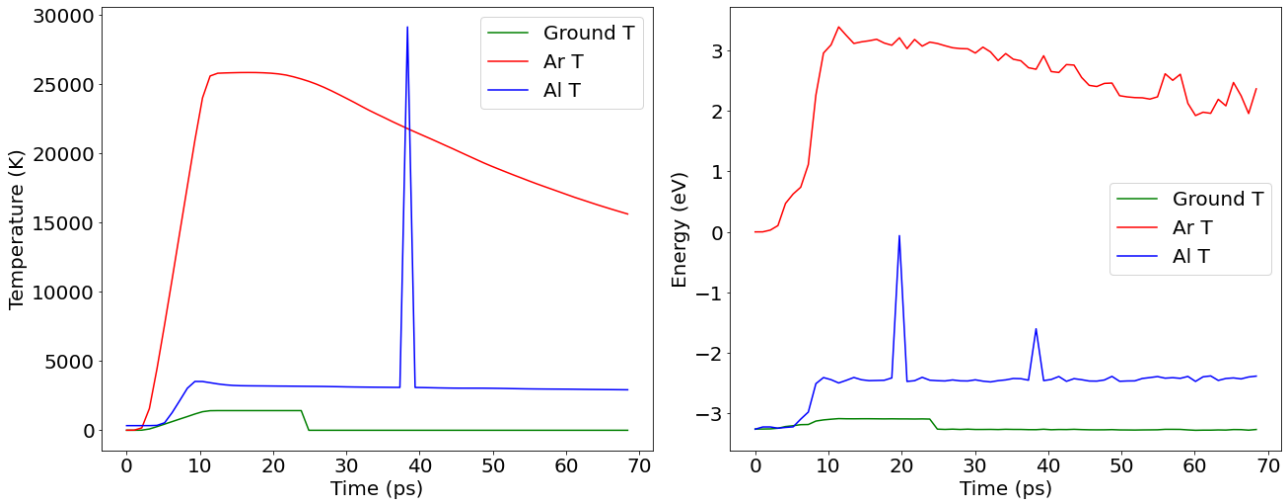

Figure 3.26: We notice one peak in the temperature chart and two peaks in the energy chart for $P = 35\,200\,\text{eV/fs}$, which we did not see in the previous simulation. This could be due to the high power that was deposed to the system, where at some point laser power interact with the Al atoms and gives enough energy to collide with another Al atom and increase insane temperature and kinetic energy, or by re-running the simulation, where when the other simulation runs, direct deposed laser power to system and direct absorbent by the high energetic atoms and start to decay their kinetic energy by collision. That is why we have two energy peaks and one temperature peak. As we can see, the temperature of Al is approximately 3500 K, whereas the ground is around 1500 K. The parameters are as follows: $v = 6.25\,\text{Å/fs}$, $\sigma_{FWHM} = 880\,\text{Å}$, $h = 900\,\text{Å}$, $1/\mu = 384.61\,\text{Å}$.

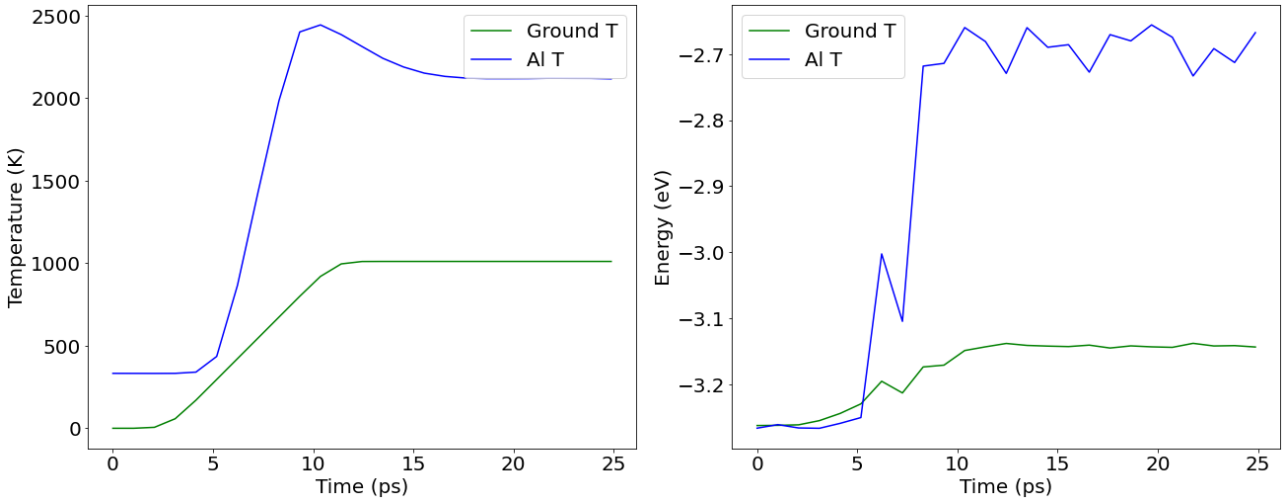

Figure 3.27: Here for the same for big sample without Ar at $P = 24\,200\,\text{eV/fs}$ for 25 ps, noticed that the same behavior of the one with Ar as in Figure 3.28 where the Ar temperature is not indicated. The same parameters are used: $v = 6.25\,\text{Å/fs}$, $\sigma_{FWHM} = 880\,\text{Å}$, $h = 900\,\text{Å}$, $1/\mu = 384.61\,\text{Å}$.

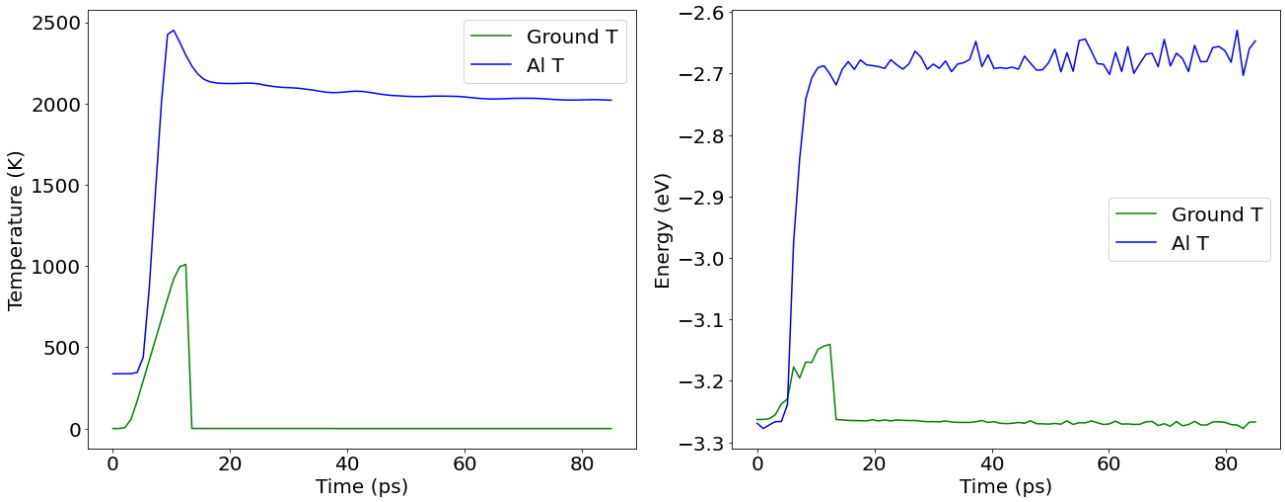

Figure 3.28: This is the identical graphic as Figure 3.25, except that the temperature Ar is not displayed in comparison to Figure 3.27. The following parameters are used: $P = 24\,200\,\text{eV/fs}$, $v = 6.25\,\text{Å/fs}$, $\sigma_{FWHM} = 880\,\text{Å}$, $h = 900\,\text{Å}$, $1/\mu = 384.61\,\text{Å}$.

Chapter 4

Conclusions and Outlooks

The aim of the present study was to simulate the MD of SLM, an AM method where a laser selectively melts one metal powder layer after another, generating the quality output. We established that the parameters analyzed and modified in this study were a good scale for melting pure Al, even when altering size and increasing the number of atoms in simulation were both samples with or without the Ar. Ar in the system makes the system more smooth and stable for the Al melt, resulting in less explosion and an improved process. Different size balls of atoms have also been researched, and how they affect larger size balls of atoms, which by increasing the size more defect will occur by spreading the atoms of the larger balls in the simulation box.

It should be noted that the powder particles have widths of a few micrometers, yet producing the required number of particles is difficult even with today's high-performance computers. To do this, the entire model is shrunk down to a few hundred angstroms in diameter and verified. In this situation, the defects that occur during SLM, as well as the approximations necessary while generating the model, are significant. The implementation of the laser settings is problematic. To be clear, the model that emerged from this work is far from complete, but the necessary requirements for developing a viable model appear to have been met.

Pure Al is utilized in a vacuum in this project and after that adding Ar to the vacuum. Although pure metals are uncommon in SLM, combined Al with other materials is often used. For the time being, Al was chosen to increase the number of known variables in this highly simplified model. While different traits and signs may presently be discerned, further development is required for more realistic models. Such as the laser absorption coefficient in Equation 2.32

and the laser power decline. A simulated cooling unit might also help enhance the accuracy of the results. The molten material has not yet hardened into its typical lattice structure. The faultless insulation created by the NVE ensemble principles also adds to the tendency of the material to continue melting long after laser irradiation.

By improving the laser parameter, the bigger size should be studied further in comparison to almost actual number atoms, and re-scale the size with random sizes and distributing the in box, as well as multiplying layers and runs of the laser on the sample in different x and y-direction positions. Should also examine Al with other types of materials that are often used in the industrial field, and how heat transitions with Al atoms affect the ground atoms, and what the effect is if it is not fixed like this study.

Appendix

Table of IMD units

Only the adjusted IMD units applicable to this study are presented here [42]:

Symbol	Unit	SI value
Length x	Å	10^{-10} m
Time t	Å $\sqrt{u/\mathrm{eV}}$	$10.18 \cdot 10^{-15}$ s
Force f	eV/Å	$1.602 \cdot 10^{-9}$ N
Stress σ	eV/Å^3	$1.602 \cdot 10^{-11}$ Pa
Mass m	u	$1.661 \cdot 10^{-27}$ kg
Fluence F	eV/Å^2	16.02 J/m^2
Temperature T	eV	11 605 K

Parameter

These are the parameters which use in param.file.

# POTENTIALS	
core_potential_file	phi.alar.pt
embedding_energy_file	f.alar.pt
atomic_e-density_file	rho.alar.pt
# CPU	
cpu_dim	32 16 16 # 8192 CPUs
# SIMULATIONS	
ensemble	nve
maxsteps	250000 # about 24h
startstep	0
timestep	0.1
box_from_header	1
checkpt_int	10000
eng_int	1
coordname	filename.config
starttemp	0.025
endtemp	0.025
# LASER	
laser_rescale_mode	1
laser_dir	0 0 1
laser_offset	165 # set to top of the sphere ≈ 160
laser_atom_vol	16.6 # Al at 300K
laser_mu	0.0143
laser_fwhm	880 # 5.5 of the sphere size
laser_power	800
laser_reflectivity	0
laser_start_position	-1600.0 101.0
laser_velocity	1.1 0.0
# laser irradiation	
pbc_dirs	1 1 1 # closed box
outfiles	folder/filename.chkpt

Bibliography

[1]S. A. Tofail, E. P. Koumoulos, A. Bandyopadhyay, S. Bose, L. O'Donoghue, and C. Charitidis, "Additive manufacturing: scientific and technological challenges, market uptake and opportunities", Materials today **21**, 22–37 (2018).

[2]S. Kurian and R. Mirzaeifar, "Deformation mechanisms of the subgranular cellular structures in selective laser melted 316l stainless steel", Mechanics of Materials **148**, 103478 (2020).

[3]C. Y. Yap, C. Chua, Z. Dong, Z. Liu, D. Zhang, L. Loh, and S. L. Sing, "Review of selective laser melting: materials and applications", Applied Physics Reviews **2**, 041101 (2015).

[4]D. Poirier, R. A. Drew, M. L. Trudeau, and R. Gauvin, "Fabrication and properties of mechanically milled alumina/aluminum nanocomposites", Materials Science and Engineering: A **527**, 7605–7614 (2010).

[5]A. S. Khan, B. Farrokh, and L. Takacs, "Effect of grain refinement on mechanical properties of ball-milled bulk aluminum", Materials Science and Engineering: A **489**, 77–84 (2008).

[6]S. Kurian and R. Mirzaeifar, "Selective laser melting of aluminum nano-powder particles, a molecular dynamics study", Additive Manufacturing **35**, 101272 (2020).

[7]D. Buchbinder, H. Schleifenbaum, S. Heidrich, W. Meiners, and J. Bültmann, "High power selective laser melting (hp slm) of aluminum parts", Physics Procedia **12**, 271–278 (2011).

[8]S. Z. Uddin, L. E. Murr, C. A. Terrazas, P. Morton, D. A. Roberson, and R. B. Wicker, "Processing and characterization of crack-free aluminum 6061 using high-temperature heating in laser powder bed fusion additive manufacturing", Additive Manufacturing **22**, 405–415 (2018).

[9]P. H. Hunenberger, "Thermostat algorithms for molecular dynamics simulations", 105–149 (2005).

[10]L. E. Murr, S. M. Gaytan, D. A. Ramirez, E. Martinez, J. Hernandez, K. N. Amato, P. W. Shindo, F. R. Medina, and R. B. Wicker, "Metal fabrication by additive manufacturing using laser and electron beam melting technologies", Journal of Materials Science and Technology **28**, 1–14 (2012).

[11]D. Herzog, V. Seyda, E. Wycisk, and C. Emmelmann, "Additive manufacturing of metals", Acta Materialia **117**, 371–392 (2016).

[12]B. Zhang, H. Liao, and C. Coddet, "Effects of processing parameters on properties of selective laser melting mg-9 precent al powder mixture", Materials and Design **34**, 753–758 (2012).

[13]E. Louvis, P. Fox, and C. J. Sutcliffe, "Selective laser melting of aluminium components", Journal of Materials Processing Technology **211**, 275–284 (2011).

[14]K. Stevenson, "Survey Indicates Massive Growth in Industrial 3D Printing", Fabbaloo (2019).

[15]Wikipedia, *Fused Deposition Modeling*, (2021) https://de.wikipedia.org/wiki/Fused_Deposition_Modeling.

[16]D. Klein, "Klassische Molekulardynamiksimulation der Laserablation von Silizium unter Verwendung von Tersoff-Potentialen", (2013).

[17]J. Stadler, R. Mikulla, and H.-R. Trebin, "IMD: A Software Package for Molecular Dynamics Studies on Parallel Computers", International Journal of Modern Physics C **08**, 1131–1140 (1997).

[18]B. Nagarajan, Z. Hu, X. Song, W. Zhai, and J. Wei, "Development of micro selective laser melting: the state of the art and future perspectives", Engineering **5**, 10.1016/j.eng.2019.07.002 (2019).

[19]T. DebRoy, H. Wei, J. Zuback, T. Mukherjee, J. Elmer, J. Milewski, A. Beese, A. Wilson-Heid, A. De, and W. Zhang, "Additive manufacturing of metallic components - process, structure and properties", Progress in Materials Science **92**, 112–224 (2018).

[20]W. J. Sames, F. A. List, S. Pannala, R. R. Dehoff, and S. S. Babu, "The metallurgy and processing science of metal additive manufacturing", International Materials Reviews **61**, 315–360 (2016).

[21]W. J. Sames, F. A. List, S. Pannala, R. R. Dehoff, and S. S. Babu, "The metallurgy and processing science of metal additive manufacturing", International Materials Reviews **61**, 315–360 (2016).

[22]M. S. Daw, S. M. Foiles, and M. I. Baskes, "The embedded-atom method: a review of theory and applications", Materials Science Reports **9**, 251–310 (1993).

[23]Z. Y. Hou, K. J. Dong, Z. A. Tian, R. S. Liu, Z. Wang, and J. G. Wang, "Cooling rate dependence of solidification for liquid aluminium: a large-scale molecular dynamics simulation study", Phys. Chem. Chem. Phys. **18**, 17461–17469 (2016).

[24]M. Mendelev, M. Kramer, C. Becker, and M. Asta, "Analysis of semi-empirical interatomic potentials appropriate for simulation of crystalline and liquid al and cu", Philosophical Magazine **88**, 1723–1750 (2008).

[25]C. A. Becker, F. Tavazza, Z. T. Trautt, and R. A. Buarque de Macedo, "Considerations for choosing and using force fields and interatomic potentials in materials science and engineering", Current Opinion in Solid State and Materials Science **17**, Frontiers in Methods for Materials Simulations, 277–283 (2013).

[26]S. D. Brown, R. Tauler, and B. Walczak, *Comprehensive chemometrics: chemical and biochemical data analysis* (Elsevier, 2020).

[27]H. Kumar and P. Maiti, "Introduction to molecular dynamics simulation", in (Jan. 2011), pp. 161–197.

[28]C. Maghfiroh, A. Arkundato, Misto, and W.Maulina, "Parameters epsilon and sigma of lennard-jones for fe, ni, pb for potential and cr based on melting point values using the molecular dynamics method of the lammps program", Journal of Physics: Conference Series **1491**, 012022 (2020).

[29]J. Hajnys, M. Pagac, J. Mesicek, J. Petru, and F. Spalek, "Research of 316l metallic powder for use in SLM 3d printing", Advances in Materials Science **20**, 5–15 (2020).

[30]J. N. Glosli, D. F. Richards, K. J. Caspersen, R. E. Rudd, J. A. Gunnels, and F. H. Streitz, "Extending stability beyond CPU millennium: a micron-scale atomistic simulation of Kelvin-Helmholtz instability", 1–11 (2007).

[31]J. N. Glosli, D. F. Richards, K. J. Caspersen, R. E. Rudd, J. A. Gunnels, and F. H. Streitz, "Extending stability beyond CPU millennium: a micron-scale atomistic simulation of Kelvin-Helmholtz instability", 1–11 (2007).

[32]A. Munster, "Statistical thermodynamics", Springer-Verlag (1974).

[33]M. A. und D. Tildesley, "Computer simulation of liquids", 1. Aufl. Oxford university press, 46 (1989).

[34]E. Eisfeld, "Molekulardynamische simulationen der laserablation an aluminium unter einbeziehung von plasmaeffekten", 22–25 (2020).

[35]J. A. Z. u. a., "Evaluation of continuum stress in atomistic simulation", Computational Fluid and Solid Mechanics 2003, 804–807 (2003).

[36]V. Z. u. a., "Simulations of surface stress effects in nanoscale single crystals", Modelling and Simulation in Materials Science and Engineering, 6 (2018).

[37]S. Plimpton, "Fast parallel algorithms for short-range molecular dynamics", Journal of Computational Physics **117**, 1–19 (1995).

[38]A. Stukowski, "Visualization and analysis of atomistic simulation data with OVITO - the open visualization tool", Modelling and Simulation in Materials Science and Engineering **18**, 015012 (2009).

[39]bliepp, *Imd cookie cutter*, (2020) https://github.com/bliepp/imd_cookie_cutter.

[40]D. Rapp, "Laserablation an AlNi-Verbindungen", (2014).

[41]Author, *Aluminum – melting point – boiling point*, (2021) https://www.nuclear-power.com/aluminum-melting-point-boiling-point/.

[42]S. Sonntag, "Computer simulations of laser ablation from simple metals to complex metallic alloys", 10.18419/opus-5016 (2011).